



HAL
open science

Study of the hydrogen escape rate at Mars during Martian years 28 and 29 from comparisons between SPICAM/Mars express observations and GCM-LMD simulations

Jean-Yves Chaufray, Francisco Gonzalez-Galindo, Miguel A. Lopez-Valverde,
François Forget, Eric Quémerais, Jean-Loup Bertaux, Franck Montmessin,
Michael Chaffin, Nicholas Schneider, John T. Clarke, et al.

► To cite this version:

Jean-Yves Chaufray, Francisco Gonzalez-Galindo, Miguel A. Lopez-Valverde, François Forget, Eric Quémerais, et al.. Study of the hydrogen escape rate at Mars during Martian years 28 and 29 from comparisons between SPICAM/Mars express observations and GCM-LMD simulations. *Icarus*, 2021, 353 (January), pp.113498. 10.1016/j.icarus.2019.113498 . insu-02343214

HAL Id: insu-02343214

<https://insu.hal.science/insu-02343214>

Submitted on 19 Nov 2020

HAL is a multi-disciplinary open access archive for the deposit and dissemination of scientific research documents, whether they are published or not. The documents may come from teaching and research institutions in France or abroad, or from public or private research centers.

L'archive ouverte pluridisciplinaire **HAL**, est destinée au dépôt et à la diffusion de documents scientifiques de niveau recherche, publiés ou non, émanant des établissements d'enseignement et de recherche français ou étrangers, des laboratoires publics ou privés.

1 **Study of the hydrogen escape rate at Mars during Martian years 28 and 29 from comparisons between**
2 **SPICAM/Mars Express observations and GCM-LMD simulations**

3 Chaufray, J-Y¹, F. Gonzalez-Galindo², M.A. Lopez-Valverde², F. Forget³, E. Quémerais¹, J-L. Bertaux¹, F.
4 Montmessin¹, M. Chaffin⁴, N. Schneider⁴, J.T. Clarke⁵, F. Leblanc¹, R. Modolo¹, R.V. Yelle⁶

5 ¹*LATMOS, CNRS, Guyancourt, France*, ²*IAA, CSIC, Granada, Spain*, ³*LMD, CNRS, Paris, France*, ⁴*LASP,*
6 *Boulder, CO, USA*, ⁵*Boston University, Boston, MA, USA*, ⁶*University of Arizona, Tucson, AZ, USA*

7
8 Abstract

9
10 We have simulated the 3D atomic hydrogen density in the Martian upper atmosphere and associated Jeans escape rate
11 during Martian years 28 and 29. The coronal Lyman- α brightness is computed using a 3D radiative transfer model
12 which accounts for the monthly average hydrogen density for these two years and is compared to a large set of
13 observations by Mars Express/SPICAM. The simulated brightness is generally in good agreement with the
14 observations for $L_s < 230^\circ$ and $L_s > 330^\circ$ for Martian year 28 and $L_s < 270^\circ$, $L_s > 340^\circ$ for Martian year 29, but the
15 model strongly underestimated the brightness for $230 < L_s < 330^\circ$ for Martian year 28 and $270 < L_s < 340^\circ$ for
16 Martian year 29. In these simulations the transport of water vapor contributes to the production of hydrogen at high
17 altitudes during southern summer. A possible explanation for the model discrepancy is an underestimate of this water
18 transport, associated with an underestimate of the hygropause altitude and/or an underestimate of the supersaturation
19 of the mesosphere. Considering this discrepancy, we estimate the hydrogen escape rate during these two Martian
20 years to vary by almost two orders of magnitude, between $\sim 10^{25}$ to $6 \times 10^{26} \text{ s}^{-1}$ (equivalent to a global layer of water
21 ~ 33 to 2000 mm deep every billion years), in agreement with the seasonal variations estimated directly from the fit
22 of the SPICAM observations during the Martian year 28 by Chaffin et al. (2014). Our analysis suggests that
23 episodic dust storms and associated enhancements at high altitude near perihelion are a major factor in the H escape
24 estimates averaged over one martian year or longer periods, but the accumulated water lost at this rate for 4 billions
25 years is much lower than the amount of water needed to form the flow channels observed on Mars.

26 1) Introduction

27
28 Several geologic and mineralogic observations indicate that Mars was not always as dry as it is today (e.g. Bibring et
29 al. 2006, Bishop et al. 2008, Hynek et al. 2010). The fate of the water is still unknown, but substantial amounts could
30 have escaped into the interplanetary medium in the form of atomic hydrogen (Jakosky et al. 2018). So, understanding

31 of how water currently escapes from Mars is necessary to investigate the long-term evolution of the Martian climate.
32 Recent observations suggest that the amount of exospheric hydrogen at Mars has important seasonal variations, with
33 a larger abundance during southern summer (Chaffin et al. 2014, Clarke et al. 2014, 2017, Bhattacharyya et al. 2015).
34 This increase of the hydrogen density should be associated with an increase of the hydrogen Jeans escape. These
35 seasonal variations have a large impact on the plasma environment of Mars (Bertucci et al. 2013, Yamauchi et al.
36 2015, Romanelli et al. 2015, Halekas 2017, Rahmati et al. 2018), and could be driven by large amounts of water
37 vapor in the mesosphere, as observed by Mars Express/SPICAM (Maltagliati et al. 2017, Fedorova et al. 2018),
38 during dust storm season (Chaffin et al. 2017, Heavens et al. 2018). Using the Global Circulation Model of
39 Laboratoire de Météorologie Dynamique (GCM-LMD) (Forget et al. 1999, Gonzalez-Galindo et al. 2009, 2015), we
40 were able to simulate seasonal variations of the hydrogen escape, but with a lower range than derived from
41 observations (Chaufray et al. 2015a). In order to better characterize the hydrogen exosphere of Mars and the
42 variability of hydrogen escape, we performed a detailed study of the Martian years 28 and 29, and compared the
43 simulated brightness to a large SPICAM Lyman- α dataset during the same two years. The year number used in this
44 study follows the convention chosen by Clancy et al. (2000) with April 11 1955 ($L_s=0^\circ$) chosen as the beginning of
45 the Martian year 1.

46 The data used in this study is described in section 2. In section 3, we present our 3D simulated Lyman- α emissions
47 corresponding to the Martian years 28 and 29, which are obtained by coupling several models. The comparisons
48 between the observed and simulated Lyman- α profiles are presented in section 4 and the possible origin of the
49 discrepancy is discussed in section 5, followed by conclusions in the last section.

50 2) Observations

51
52 The Spectroscopy for Investigation and Characterization of the Atmosphere of Mars (SPICAM) is a dual ultraviolet
53 and infrared spectrometer aboard Mars Express (Bertaux et al. 2006, Montmessin et al. 2017). The ultraviolet channel
54 uses an optical entrance of 4 cm diameter feeding an off-axis parabolic mirror which focuses the observed scene at
55 the focal plane. The instantaneous field of view (IFOV) is limited at the focal point of the parabolic mirror by a 50
56 μm wide retractable slit that extends over an angular aperture of 2.8° , equivalent to about two pixels on the UV
57 detector. In the upper most portion of the slit, a 10 times wider aperture allows for the observations of fainter sources
58 at the expense of degraded spectral resolution.

59 In principle, SPICAM can record 288 spatially resolved spectra along the slit. However, to save data volume
60 transmission, only 5 spectra are transmitted each second. For all the observations presented here, the spectra are the
61 sum of 32 individual CCD line spectra forming 5 adjacent spatial bins of 0.32° each, starting from the CCD line Y_0 .
62 The wavelength range of the UV channel is 118 – 320 nm and includes the strong hydrogen Lyman- α emission line at
63 121.6 nm. This emission line is produced by resonant scattering of solar photons by hydrogen atoms in the Martian
64 upper atmosphere. Such emission is observed over several Martian radii as a signature of the extended hydrogen
65 exosphere of Mars (Chaufray et al. 2008).

66 We selected several observations obtained during the Martian years 28 (from 22 Jan 2006 to 9 Dec 2007) and 29
67 (from 10 Dec 2007 to 26 Oct 2009) performed by the UV spectrograph SPICAM on Mars Express, including those
68 studied by Chaffin et al. (2014). During this period the UV channel exhibited an anomalous image intensifier
69 behavior, leading to sporadic changes of the high voltage during a sequence of observations (Montmessin et al.
70 2017). We selected by visual inspection the observations least affected by this behavior. A cleaning procedure has
71 been developed to flag the UV channel spectra affected by these high voltage spikes (Montmessin et al. 2017). All
72 these flagged spectra have been removed from use in this study.

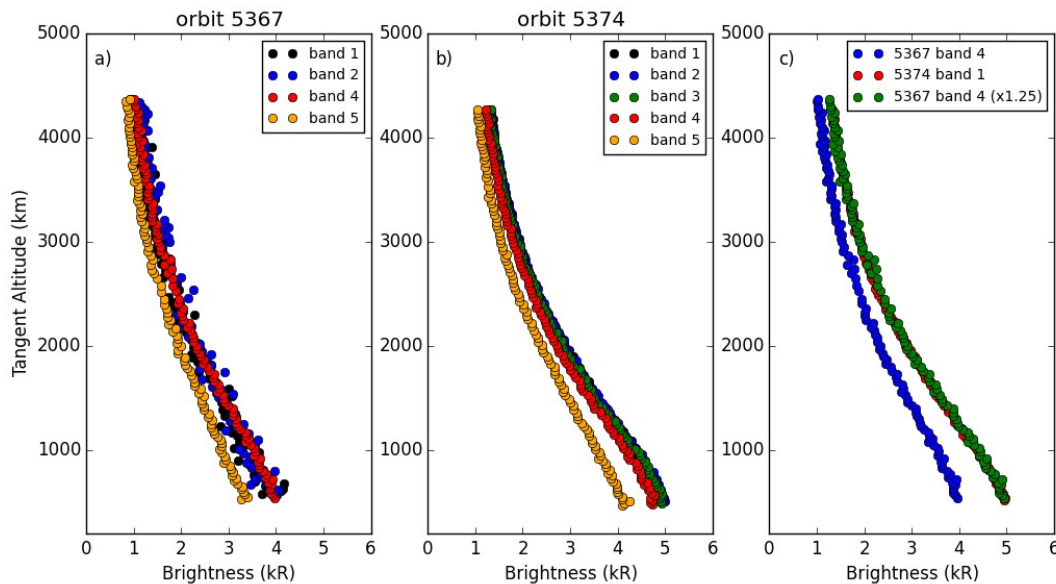
73 The list of observations used for this study is summarized in Tables 1 and 2 in the Appendix.

74 Some of the observations were performed without the slit, while others were performed with the slit. Also, the 5 CCD
75 spatial bands (corresponding to a binning of 32 individual, consecutive lines) transmitted each second can differ
76 between observations. Three different configurations are used in the observations presented here. The first
77 configuration corresponds to an observation with the slit and starts from CCD line $Y_0 = 23$, the second configuration
78 also corresponds to an observation with the slit, but starts from CCD line $Y_0 = 118$, and the third configuration
79 corresponds to an observation without the slit, starting from CCD line $Y_0 = 118$.

80 For the first configuration, all the transmitted bands correspond to the part of the CCD in front of the narrow part of
81 the slit, so we chose band 5, which is close to the center of the CCD (lines 118- 149). For the second configuration,
82 the last two bands correspond to the part of the CCD in front of the large part of the slit. The signal to noise ratio is
83 generally better, and straylight near 132 and 143 nm discussed by Leblanc et al. (2006) and Chaufray et al. (2009) is
84 not detected in those bands. Therefore, we chose band 4 (lines 214-245), which is more sensitive than band 5 by
85 about 20% (Fig. 1a). For the last configuration without the slit, we chose band 1, which corresponds to the same CCD
86 lines as configuration 1 (lines 118-149), but is slightly different (by about 5%) than the derived brightness from band

87 4 (lines 214-245) (Fig. 1b). As shown in Fig. 1, the signal to noise ratio of the derived brightness profile is very good
 88 and trying to improve it by using the 5 transmitted bands will not change our results since the calibration uncertainty
 89 is larger than the standard deviation of the measurement.

90

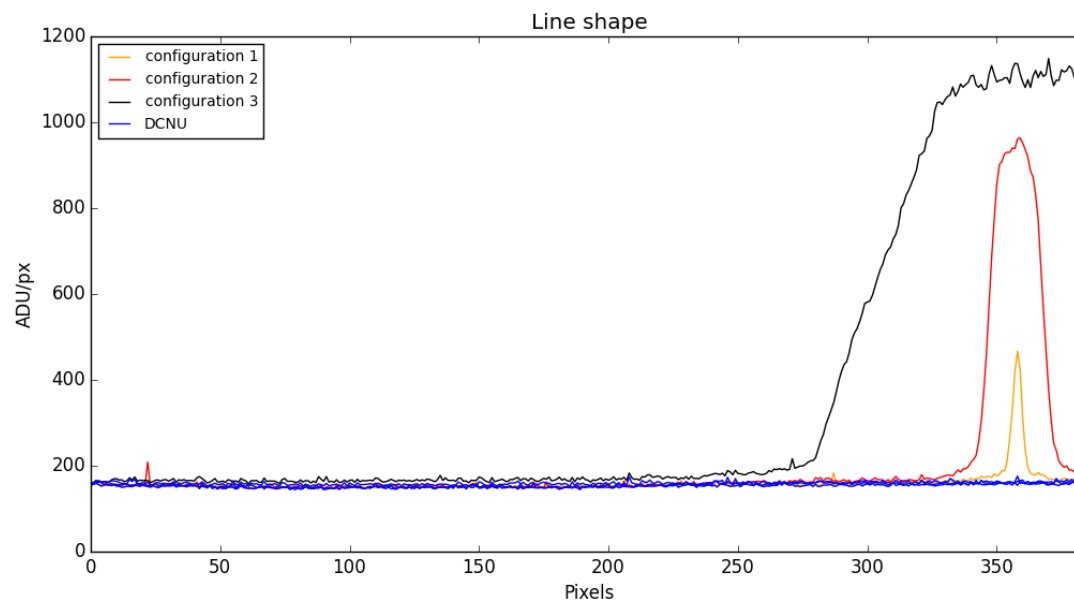


91 *Fig. 1 : a) Brightness profiles derived from Mars Express orbit 5367 with the slit over the first 2 and last 2*
 92 *transmitted bands of the CCD. b) Brightness profiles derived from Mars Express orbit 5374 without the slit over the*
 93 *5 transmitted bands. c) Comparison between the profiles derived from the two orbits over the bands used in this*
 94 *study considering a 1.25 factor for the observations with the slit*

95 Observations with very similar geometries (orbits 5367 and 5374 for example, Fig. 1) obtained with and without the
 96 slit, indicate a systematic $\sim 20\%$ underestimate of the derived brightness with the slit compared to the observations
 97 without the slit (Fig. 1b). 5% could be attributed to the different CCD lines as suggested by Fig. 1b. The rest of the
 98 difference could come from the method used to integrate the spectral line, neglecting the extended spectral wings, or
 99 in a continuum background subtraction. Therefore, to summarize, the brightness measured by configuration 3 is used
 100 as a reference, and a correction by 20% is applied to the brightness measured in configuration 1 and a correction of
 101 25% is applied to the brightness measured by configuration 2. Examples of Lyman- α vertical profiles are displayed in
 102 Fig. 1.

103 The spectral shape of the Lyman- α line measured for each configuration is displayed in Fig. 2. For the first two
 104 configurations, the brightness is computed by integration over the line profile after subtraction of a residual linear
 105 background (Chaufray et al. 2008). For the third (slitless) configuration, the average number of counts per pixel is
 106 computed and converted to Rayleighs using the solid angle defined by one pixel. All spectra have been corrected for

107 the offset and Dark Charge non-uniformity (DCNU) (see Bertaux et al. 2006 for more details).



108

109 *Fig. 2 Spectral shape of the Lyman- α line measured for the three configuration used in the paper. These spectral*
110 *profile correspond to the average observation between 2000 and 2200 km from observation 5367 (narrow slit :*
111 *configuration 1 and large slit : configuration 2) and observation 5374 (no slit : configuration 3). A sapphire filter is*
112 *glued above the CCD MgF₂ input window, preventing Lyman- α photons to reach pixels < 250 without slit (Bertaux et*
113 *al. 2006). With the slit, the linewidth is constrained by the slit size. The Dark charge non-uniformity (DCNU) is also*
114 *indicated in blue and is very similar for these three measured spectra.*

115 Such a systematic uncertainty is in the range of the absolute calibration of the instrument from star observations
116 (Montmessin et al. 2017). Therefore, in this study we focus on systematic differences between the observations and
117 the simulations which are >25%, as well as the differences in the shape of the observed and simulated vertical
118 variations.

119 **3) Models**

120

121 To simulate the hydrogen corona of Mars during Martian years 28 and 29, we used three models. The first model is
122 the GCM-LMD describing the Martian atmosphere from the surface to the exobase (Forget et al. 1999, Gonzalez-
123 Galindo et al. 2009, 2015), including the hydrogen in the thermosphere (Chaufray et al. 2015a, 2018). The second
124 model is an exospheric model considering nonuniform conditions at the exobase (hydrogen density and temperature
125 from the GCM-LMD) to derive the hydrogen density in the exosphere, based on the approach of Vidal-Madjar and
126 Bertaux 1972. The last model is a 3D Monte Carlo radiative transfer model used to simulate the resonance Lyman- α

127 spectral volume emission rate (Chaufray et al 2015b). The Lyman- α brightness is computed by formal integration of
128 the radiative transfer equation using simulated volume emission rates for the specific geometry (spacecraft position
129 and line of sight direction) of each individual observation listed in Tables 1 and 2 in Appendix A. The simulated
130 brightness is directly proportional to the solar flux at the center of the solar Lyman- α line. To derive it, we used the
131 solar brightness between 121-122 nm measured by SORCE (Rottman et al. 2006) rescaled to Mars distance, with
132 accounting for the different ecliptic longitudes of Earth and Mars as seen from the Sun. The brightness at the center
133 of the line is derived from the empirical relation given by Emerich et al. (2005). The variability of the solar flux
134 between 121 and 122 nm measured by SORCE during the full period is $\sim 10\%$, therefore uncertainty on the flux at
135 Mars, due to the different ecliptic longitudes of Mars and Earth should be at most $\sim 10\%$ but could differ from one
136 observation to the other. Due to the large CPU time required by the Monte Carlo radiative transfer simulations, it is
137 not possible to simulate the Martian Lyman- α volume emission rate with every GCM-LMD time step. In this study,
138 we consider only monthly average hydrogen for the exosphere and corona. This is another source of uncertainty in
139 the simulated brightness that prevents us from discussing differences less than a few tenths percent in the brightness
140 comparisons. This resolution is enough to discuss the seasonal variations that are important, as observed from several
141 missions (Chaffin et al. 2014, 2018, Clarke et al. 2014, Battacharyya et al. 2015, 2017).

142 **3.1) Thermospheric density**

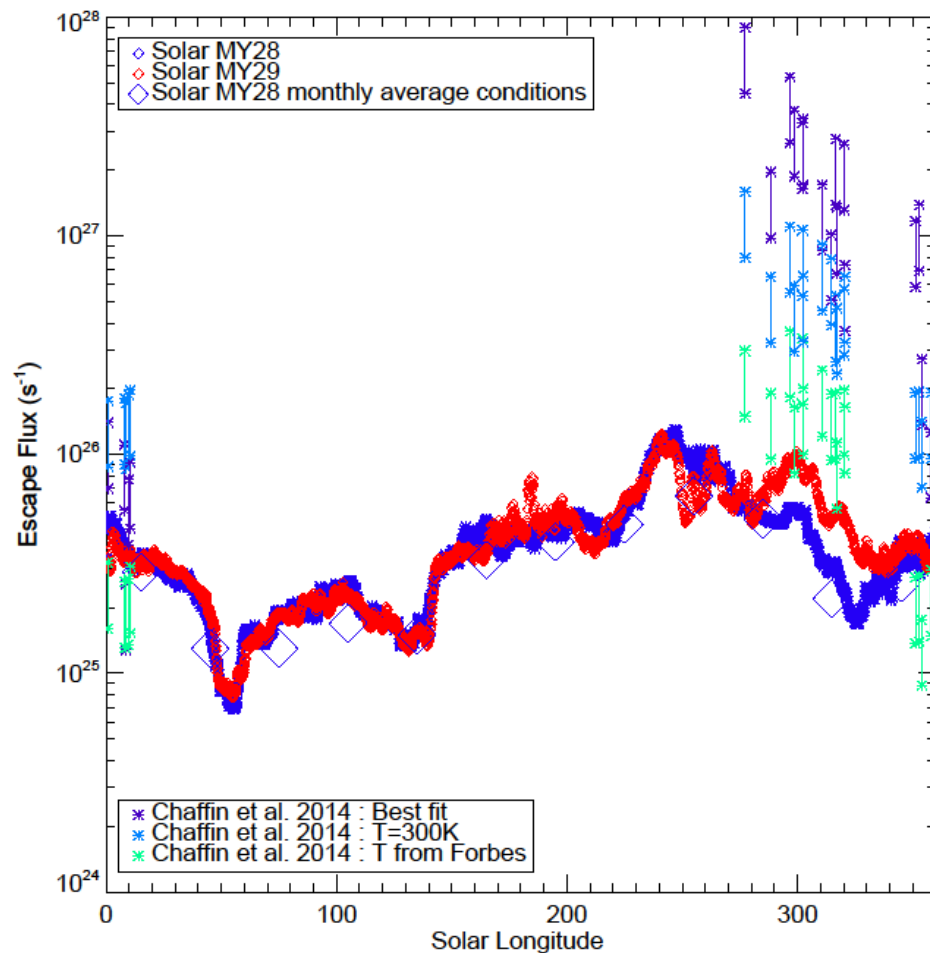
143
144 The GCM-LMD is a 3D model of the Martian atmosphere from the surface to the exobase. It is composed of a 3D
145 dynamics core which solves the fluid equations over a sphere and a physical core, describing all the physical
146 processes computed for each column. In all the simulations presented below, the horizontal resolution is 5.625° in
147 longitude and 3.75° in latitude. The dynamical time step δt is 1 sol/960. ~ 1.5 minute, and the physics time step is Δt
148 $= 5\delta t \sim 7.5$ minutes. More details on the GCM-LMD can be found in Forget et al. (1999) and Gonzalez-Galindo et al.
149 (2009, 2015). As noted in Chaufray et al. (2015a) the vertical resolution used in the molecular diffusion (2 km) can
150 lead to an uncertainty of a few tenths in the hydrogen density above 200 km, depending on the season and martian
151 year. Because we will focus on large differences between the simulated brightness and observed brightness, this
152 uncertainty as a monthly average exosphere, should not change our conclusion.

153 In these simulations, we account for the daily variations of the solar flux during the Martian year 28 and 29 as
154 computed by Gonzalez-Galindo et al. (2015). We also consider the dust scenarios of these years derived by

155 Montabone et al. (2015). We do not include the microphysical processes controlling the supersaturation presented in
156 Navarro et al. (2014), as these results, and especially the hydrogen density in the Martian thermosphere, depend on
157 model parameters not well constrained by the observations. These simulations will be discussed in section 5. We also
158 do not include the coupling with the exospheric ballistic transport developed by Chaufray et al. (2018). This coupling
159 can't be performed for a full Martian year because of the large CPU time needed. The first few studies we performed
160 indicate that the effect on the brightness should not be greater than a few tens of percent, and therefore, the
161 differences discussed in section 5 should still be present with this coupling. A study of the local time variations
162 would require such a coupling. Therefore, in this paper we will focus on the seasonal variation of the hydrogen
163 corona and escape. We only consider the hydrogen Jeans escape, computed assuming a
164 Maxwellian distribution at the upper level. Shizgal and Blackmore (1986) have shown that
165 the depletion of energetic atoms could reduce the real escape rate by a factor ~ 0.57 for an
166 exospheric temperature of 230 K and 0.53 for an exospheric temperature of 310 K, We also
167 neglect the non-thermal escape processes which should be not very efficient for atomic
168 hydrogen compared to the thermal escape rate (Krasnopolsky 2010). The non-thermal escape
169 of molecular hydrogen was discussed in Krasnopolsky (2017) and Chaufray et al. (2017)
170 and is not included in these simulations.

171 The simulated escape flux for the Martian years 28 and 29, as well as the escape flux derived from the monthly
172 average conditions for Martian year 28 are displayed on Fig.2. These variations are close to the simulated escape
173 rates for solar minimum conditions by Chaufray et al. (2015a; 2018) as expected for these Martian years.

174



175
 176 *Fig. 3 : Jeans hydrogen escape rate simulated for the Martian years 28 (blue) and 29 (red) with the GCM-LMD. The*
 177 *escape rate derived from the monthly average upper atmosphere are also indicated by the blue diamonds. The escape*
 178 *rates derived from SPICAM fit (from observations between end of Martian year 28, beginning of Martian year 29)*
 179 *using different assumptions by Chaffin et al. 2014 are also displayed. The escape flux (at/cm²/s) was converted to*
 180 *escape rate (at/s). For this conversion, we assume either a uniform flux at the exobase or a uniform flux at the*
 181 *dayside exobase and no escape flux at the nightside, leading to the range given by each vertical line.*

182 **3.2) Exospheric density**

183
 184 The hydrogen density is extended to the exosphere (above 200 km), by solving the Liouville equations from non-
 185 uniform conditions at the exobase (Vidal-Madjar and Bertaux 1972). We consider Maxwellian velocity
 186 distribution functions at the exobase using the temperature and the hydrogen density computed from the LMD-GCM
 187 reinterpolated at 200 km as done in our previous simulations (Chaufray et al. 2015a, 2018). The real distribution at
 188 the exobase should differ from a Maxwellian distribution. Due to the escaping particles, the Maxwellian distribution
 189 is truncated at velocity larger than the escape velocity ([Shizgal and Blackmore 1986](#), Boqueho et al. 2005, Terada et
 190 al., 2016). However, this truncation should not affect the ballistic distribution with a velocity lower than the escaping

191 velocity but only reduce the escape rate (Brinkmann, 1970). The Direct Simulation Monte Carlo method used by
192 Terada et al. (2016) shows that the ballistic hydrogen population is very close to the Maxwellian distribution at the
193 local temperature (see Fig 8b in Terada et al. 2016).

194 In the computation of the exospheric hydrogen density we neglect ionization loss and the effect of solar radiation
195 pressure that should be important at a few Martian radii above the altitudes scanned by the missions and the optically
196 thick region of the hydrogen corona (Beth et al. 2014).

197 **3.3) Radiative transfer model for resonance line**

198
199 The computation of the Lyman- α brightness is done in two steps, as done by numerous models (e.g., Gladstone
200 1992). In a first step, we use a 3D Monte Carlo radiative transfer model to compute the 3D volume emission rate
201 from 80 km to 50,000 km. This radiative transfer model is a 3D version of the model used by Chaufray et al. (2012,
202 2015b) to study the hydrogen corona of Venus, which accounts for angle-dependent partial frequency redistribution
203 (Lee 1982) and describes the spectral line from -5 to +5 Doppler width (at the maximum temperature at the exobase,
204 i.e., $\sim \pm 40$ m/s).

205 The brightness is then computed in a second step, rescaling the volume emission rate to the solar flux at Lyman- α at
206 the time of the observations and accounting for the geometry of each individual observation from Mars Express
207 (Chaufray et al. 2008). Twenty-four 3D volume emission rates, monthly average, corresponding to Martian months of
208 the years 28 and 29 have been computed. To reduce the CPU time, we did not simulate every line of sight for
209 each observation, but instead averaged several lines of sight (between 5 and 20) and compared the simulated
210 brightness of the average line of sight with the observed average brightness.

211 The interplanetary brightness emission is estimated for each individual observation using a 3D radiative transfer
212 model of the interplanetary emission (Qu  merais 2000). The possible uncertainty on the brightness should be small
213 ($\sim 100\%$) compared to the brightness of the Martian hydrogen corona and will not change the conclusion of this
214 study.

215 **3.4) Effect of ballistic transport in the Martian exosphere**

216
217 The effect of ballistic transport on the hydrogen density near the exobase of Mars has been recently studied
218 (Chaufray et al. 2018). This coupling has not been included in this study due to the large CPU needed to perform
219 such coupled simulations. Our first estimates indicate that considering this coupling has a small effect on the

220 simulated brightness. The Lyman- α emission line is optically thick below few thousands kilometers in altitude
 221 (Bhattacharyya et al. 2017) and therefore is sensitive to global conditions and not too significantly affected by local
 222 conditions. Ballistic transport redistributes the hydrogen atoms in the exosphere, but does not change the global
 223 amount of hydrogen in the exosphere. Therefore, it is not surprising to find a limited impact on the simulated
 224 brightness. Since the main goal of this study is to focus on the large differences between the simulations and the
 225 observations, in the next section we will neglect this effect. A more careful study of the local time variations by few
 226 tenths of the brightness as observed by MAVEN (Chaffin et al. 2015) would need to include this effect and such a
 227 study is therefore deferred to a future work.

228

229 **4) Comparisons with observations**

230 Examples of comparisons between the observed brightness and the simulated brightness at different Martian months
 231 are displayed on Fig. 4. The model reasonably reproduces the observations at $L_s = 180^\circ$, 220° and 340° but
 232 underestimates the brightness at $L_s = 280^\circ$ and does not reproduce the shape of the vertical profile. To quantify the
 233 difference between the observed and simulated brightness, we derived an optimized scale factor which needed to be
 234 applied to the observation to better reproduce the simulated profile by minimizing the function.

$$235 \quad \Delta^2 = \sum_{los} [\log(I_{obs}) + \log(A) - \log(I_{sim})]^2$$

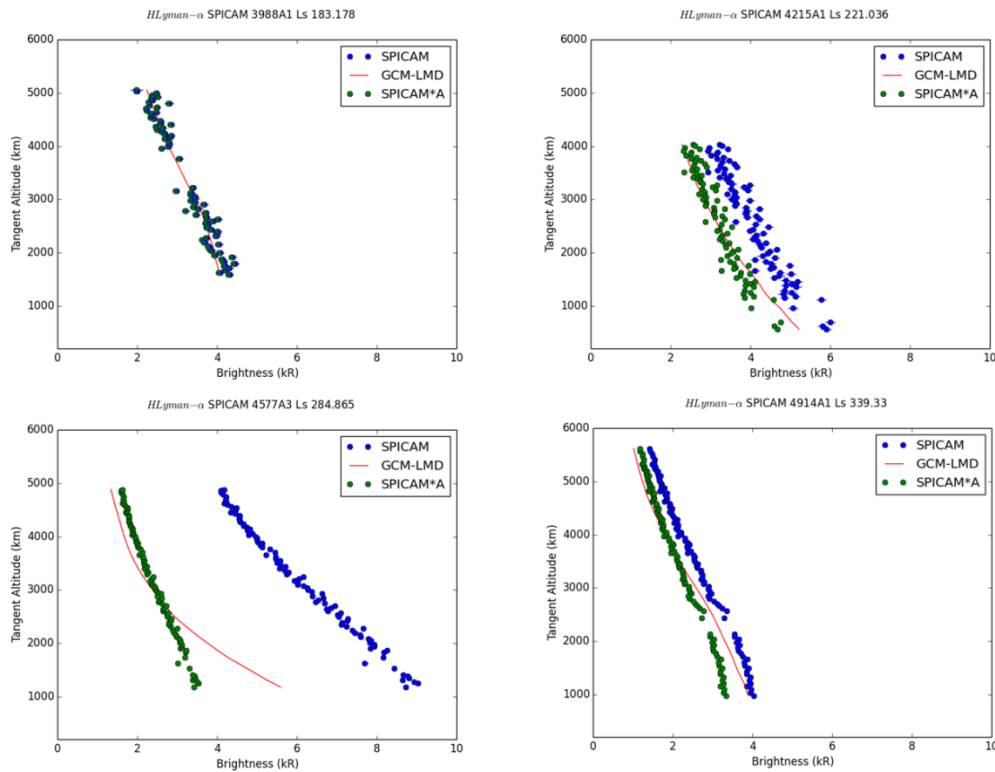
236 The minimum of the function Δ^2 is found when its derivative $\partial\Delta^2/\partial A = 0$ yielding A as

$$237 \quad \log(A) = \frac{1}{n} \sum_{los} [\log(I_{sim}) - \log(I_{los})]$$

238 The rescaled profile is also displayed on Fig.4. For the three observations at $L_s = 180^\circ$, 220° and 340° displayed in
 239 Fig. 4, this scale factor is 0.99, 0.79, and 0.82 respectively, and is in the range of possible uncertainty associated with
 240 the retrieved brightness and the solar flux at Mars or the simulation of a monthly average hydrogen corona. For the
 241 observation near $L_s = 280^\circ$, the scale factor is 0.39, which cannot be explained by the uncertainty in the retrieved
 242 brightness by SPICAM-UV.

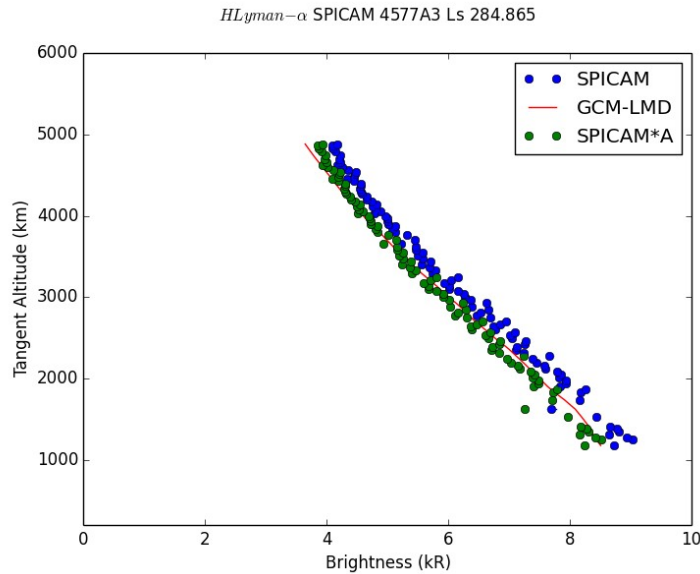
243 The difference between the simulated and the observed Lyman- α brightness indicates an important underestimate of
 244 the hydrogen density by the model, as was suggested by our first simple comparison of the escape rate derived from
 245 SPICAM by Chaffin et al. (2014) at this season (from the same set of observations) and the simulated escape rate for
 246 different solar conditions (Chaufray et al. 2015a). The shape of the simulated profile also differs from that of the

247 observed profile, confirming that the difference cannot be attributed to the absolute calibration of SPICAM or an
 248 underestimate of the solar flux at Mars and is therefore due to an underestimate of the hydrogen density at this season
 249 by our model. Observations performed simultaneously between $L_s = 331$ and 345° by HST during the Martian year
 250 28 also indicate a decrease of the hydrogen corona from this period (Clarke et al. 2014), which is consistent with the
 251 SPICAM observations.
 252 Possible explanations of this underestimate of the hydrogen content of the Martian upper atmosphere in our model
 253 will be discussed in section 5



254
 255 *Fig. 4 Examples of comparisons between the Lyman- α brightness profiles observed by SPICAM-UV (blue dots) and*
 256 *the simulated brightness profile (red line) for different solar longitude L_s during the Martian year 28.*

257 Fig. 5 displays the simulated profile corresponding to observation 4577 when the simulated hydrogen density is
 258 arbitrarily multiplied by a factor 6. In that case, the simulated profile is in better agreement with the observation and
 259 the simulated shape of the profile is consistent with the observed shape, confirming the difference is likely due to an
 260 underestimate of the hydrogen density by the model.

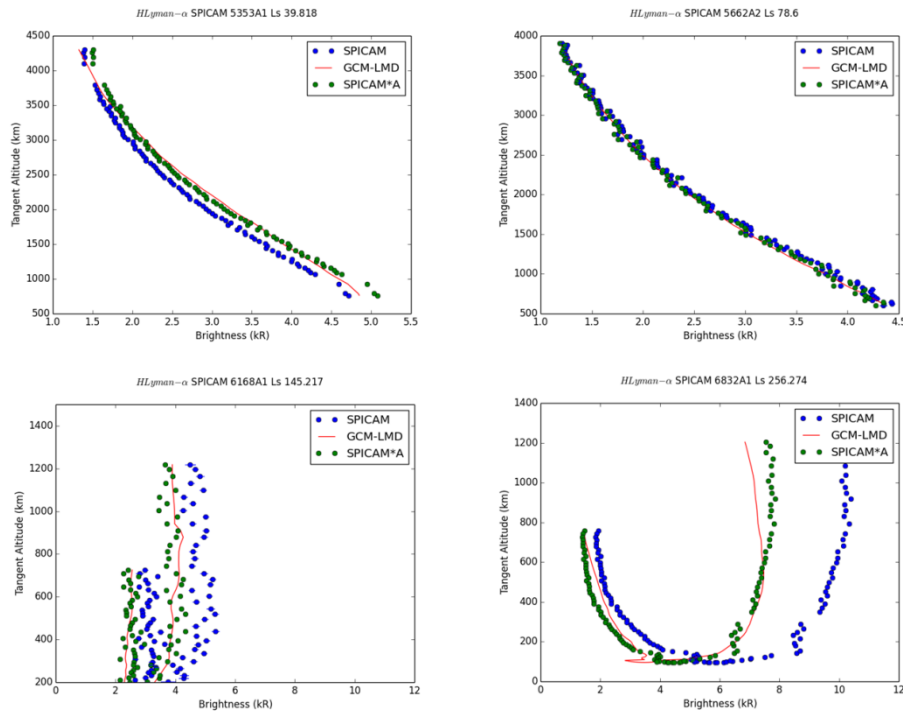


262 *Fig. 5 Simulated Lyman- α brightness profile for orbit #4577 with a simulated hydrogen density multiplied by 6*
 263 *w.r.t. the normal model, compared to the SPICAM*

264 Examples of comparisons between the observed brightness and the simulated brightness at different Martian months
 265 for Martian year 29 are displayed on Fig. 6. The model reasonably reproduces the observations at Ls near 40° , 80°
 266 (the best comparison for the full set of observations), and to a lesser extent, near 145° , but fails to reproduce
 267 the observation near Ls= 255° . The observation at Ls= 255° corresponds to a grazing limb observation with a tangent
 268 altitude decreasing at the nightside (brightness $< 4\text{kR}$) reaching a minimum altitude near 100 km and increasing on
 269 the dayside where the Lyman-alpha brightness is large, $\sim 10\text{kR}$.

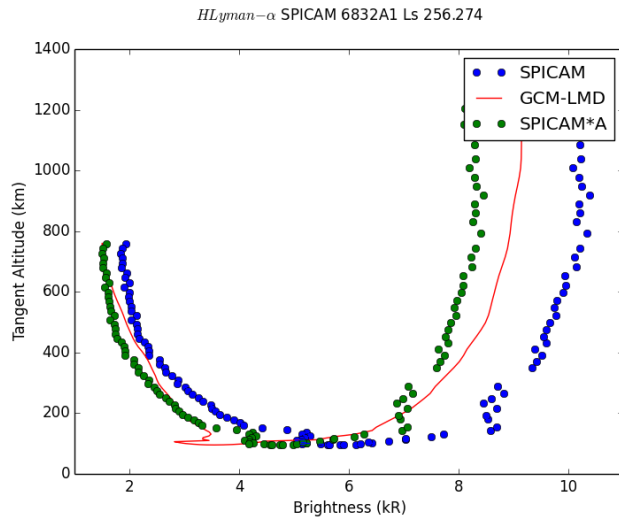
270 For the Martian year 29, we derive an optimized scale factor A for each observation. The scale factors are 1.08, 0.98,
 271 0.81 and 0.75 for the four profiles displayed on Fig. 5., confirming that the model underestimates the brightness near
 272 summer southern solstice. While the factor 0.75 is close to the reasonable value, it corresponds to a large difference
 273 in term of hydrogen density, due to the large brightness ($\sim 10\text{kR}$) and the non-linearity between the density and the
 274 brightness for an optically thick emission.

275 As for the Martian year 28, we performed another simulation with the hydrogen density arbitrarily multiplied by 6
 276 for the observation #6832. Fig. 7 shows that the agreement is slightly better, as expected, but the brightness is still
 277 underestimated. But the remaining difference is less than 1kR and could be due to the deuterium emission not
 278 included in our simulations, this could possibly be important at this season at these low altitudes (Clarke et al. 2017,
 279 Chaffin et al. 2018).



280

281 *Fig. 6 Examples of comparisons between the Lyman- α brightness profiles observed by SPICAM- UV (blue dots) and*
 282 *the simulated brightness profile (red line) for different solar longitude Ls during the Martian year 29*



283

284 *Fig. 7 Simulated Lyman- α brightness profile for orbit #6832 with a simulated hydrogen density multiplied by 6 w.r.t.*
 285 *the normal model, compared to the SPICAM*

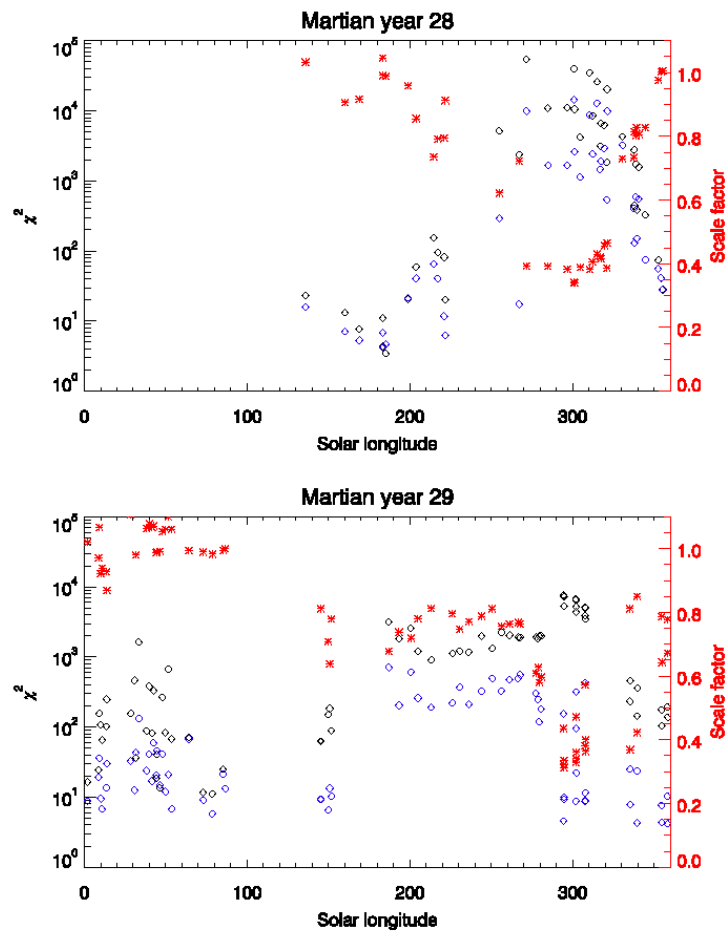
286 For each observation from Martian years 28 and 29, we derive a scale factor and compute the χ^2
 287 value for the observed and the rescaled profiles given by :

$$288 \quad \chi^2 = \frac{1}{n} \sum_{los} \frac{[B * I_{obs} - I_{sim}]^2}{B^2 \sigma_{obs}^2}$$

289 with $B = 1$ for the observed profile and $B = A$ for the rescaled profile.

290 Fig.8 displayed the χ^2 value versus Ls, including all observations given in Table 1, as well as the scale factor A

291 derived from each observation



292

293 *Fig. 8 χ^2 variations (black diamond, left scale) for the Martian year 28 (top) and Martian year (29), and best scale*
294 *factor variations (red crosses, right scale), with the associated χ^2 values (blue diamonds).*

295

296 The full set of observations confirm the conclusion derived from the few examples shown in Figs. 4 and 6. The
297 simulated profiles are in reasonable agreement with the observed profile when $\chi^2 < 100$, and the scale factor is larger
298 than 0.8 ($L_s < 230^\circ$ and $L_s > 330^\circ$) for Martian year 28, and $L_s < 150^\circ$ and $L_s > 340^\circ$ for Martian year 29). The scale
299 factor reaches the smallest values $\sim 0.3-0.4$ for $L_s = 250^\circ - 330^\circ$ for both years, meaning the model strongly
300 underestimates the hydrogen density for this season. For Martian year 28, even if the absolute brightness was
301 rescaled, the shape of the profile would not be well reproduced as indicated by the large value of χ^2 (see also Fig. 4
302 bottom left) when the optimized scale factor is included. To reproduce the observed profile, the simulated hydrogen
303 density should be multiplied by ~ 6 as shown for orbit 4577 in Fig. 5.

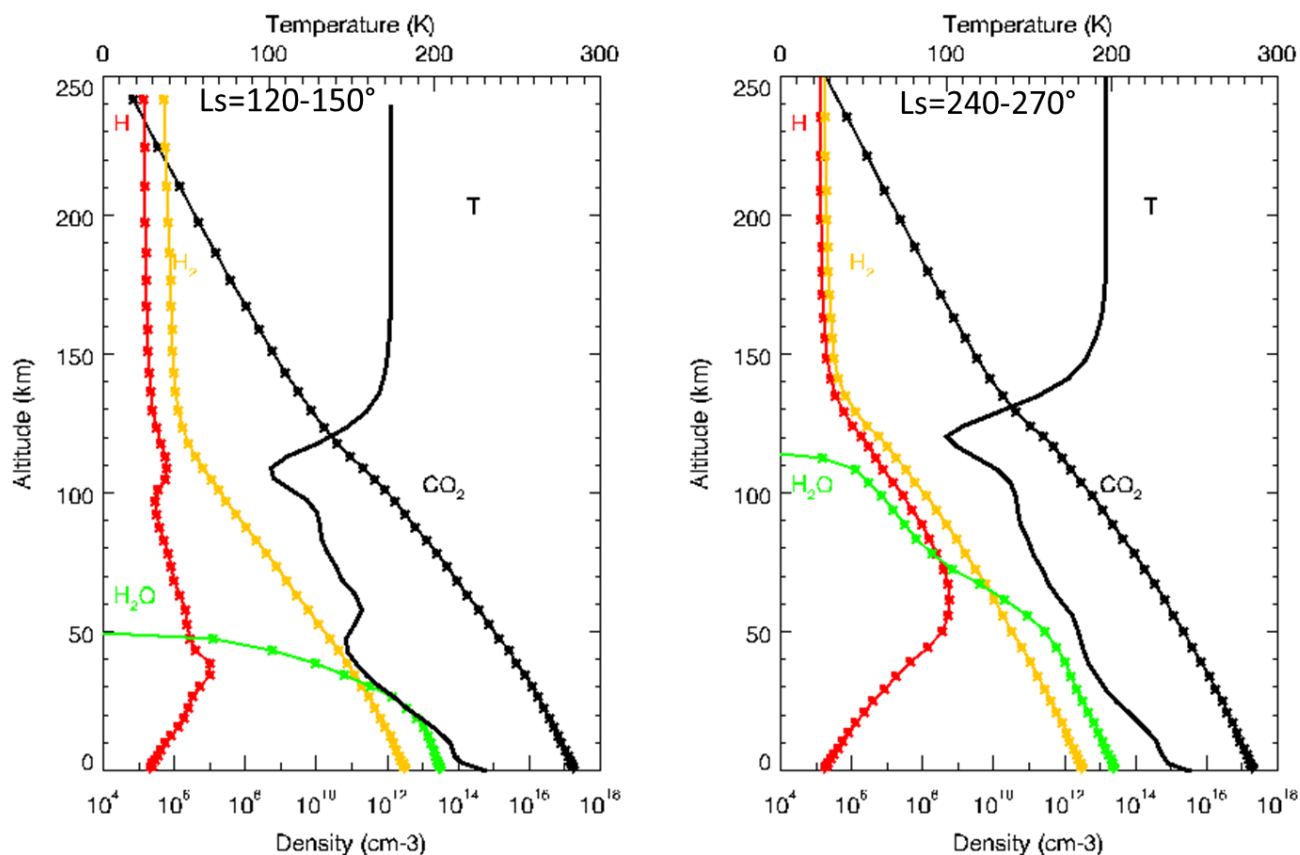
304 At L_s near 0° (observation #5070), Chaffin et al. (2014) was able to fit the observed profile with an escape flux
305 between 1×10^7 and $1 \times 10^8 \text{ cm}^{-2}\text{s}^{-1}$, corresponding to a total escape rate $\sim 1.6 \times 10^{25}$ and $1.6 \times 10^{26} \text{ s}^{-1}$ if we assume a

306 uniform escape flux at the exobase in agreement with our simulated escape rate equal to $4 \times 10^{25} \text{ s}^{-1}$ at this season (Fig.
307 3). The escape flux simulated is not uniform and larger at the dayside than nightside (Chaufray et al. 2015a). If we
308 integrate only the escape flux at the dayside to derive the escape rate, then all the derived escape rate from SPICAM
309 shown in Fig. 3 should be divided by two. In that case, the observations near $L_s=0^\circ$ are still in agreement with our
310 simulations. The two other observations detailed in Chaffin et al. (2014) (observation #4646 and #4501) are not
311 reproduced by our simulations and the escape rate derived by Chaffin et al. (2014) was between 2×10^8 and $5 \times 10^9 \text{ cm}^{-2}$
312 s^{-1} (3×10^{26} and $8 \times 10^{27} \text{ s}^{-1}$) for observation #4501 ($L_s = 271^\circ$) and between 1×10^8 and $2 \times 10^9 \text{ cm}^{-2} \text{ s}^{-1}$ ($1.6 \times 10^{26} \text{ s}^{-1} -$
313 $3.2 \times 10^{27} \text{ s}^{-1}$) for observation #4646 ($L_s = 296^\circ$), larger than our simulated escape flux of $\sim 10^{26} \text{ s}^{-1}$ at these periods
314 (Fig. 2). These high values would be in better agreement with the model escape flux if the simulated hydrogen
315 density was increased by a factor ~ 6 as suggested by our simple density rescale.

316 **5) Discussion**

317 The hydrogen density in the Martian upper atmosphere simulated for Martian years 28 and 29 is in general in
318 reasonable agreement with the SPICAM observations suggesting that the main source processes of atomic hydrogen
319 are included in these simulations during most of the Martian year, except near southern summer solstice ($L_s \sim 270^\circ$).
320 At this period, the hydrogen density and the escape rate are likely underestimated by a factor ~ 6 .
321 At this period, deuterium Lyman- α could contribute partly to the brightness, especially in the thermosphere / lower
322 exosphere as shown by MAVEN/IUVS (Clarke et al. 2017), for example for orbits 6500s, 6600s and 6700s (Fig. 6
323 bottom right). However, the deuterium brightness measured by MAVEN/IUVS during Martian year 32 is less than 1
324 kRayleigh and decreases quickly with altitude, becoming negligible above 300 km. Such a low brightness is
325 insufficient to explain the discrepancy between the model and the observations. Substantial amounts of water vapor at
326 high altitude in the mesosphere has been detected by SPICAM at this season (Maltagliati et al. 2013, Fedorova et al.
327 2018). The water vapor could be photodissociated and contribute to an increase in the hydrogen density in the
328 Martian thermosphere and exosphere, as well as the hydrogen escape (Chaffin et al. 2017). The MAVEN/NGIMS
329 ionospheric observation above 150 km near the same season (Martian year 32) suggested a water vapor mixing ratio
330 of only 0.4 ppb at 80 km, in order to avoid the loss of observed HCO^+ by H_2O reactions (Fox et al. 2015), but has
331 been recently questioned by another model (Krasnopolsky 2019). In this study, the water vapor density profile was
332 assumed to be close to a diffusion equilibrium profile. Recently, Heavens et al. (2018) suggested that the increase of
333 the hygropause altitude due to dust storms could lead to an increase of the hydrogen density (and escape) in the

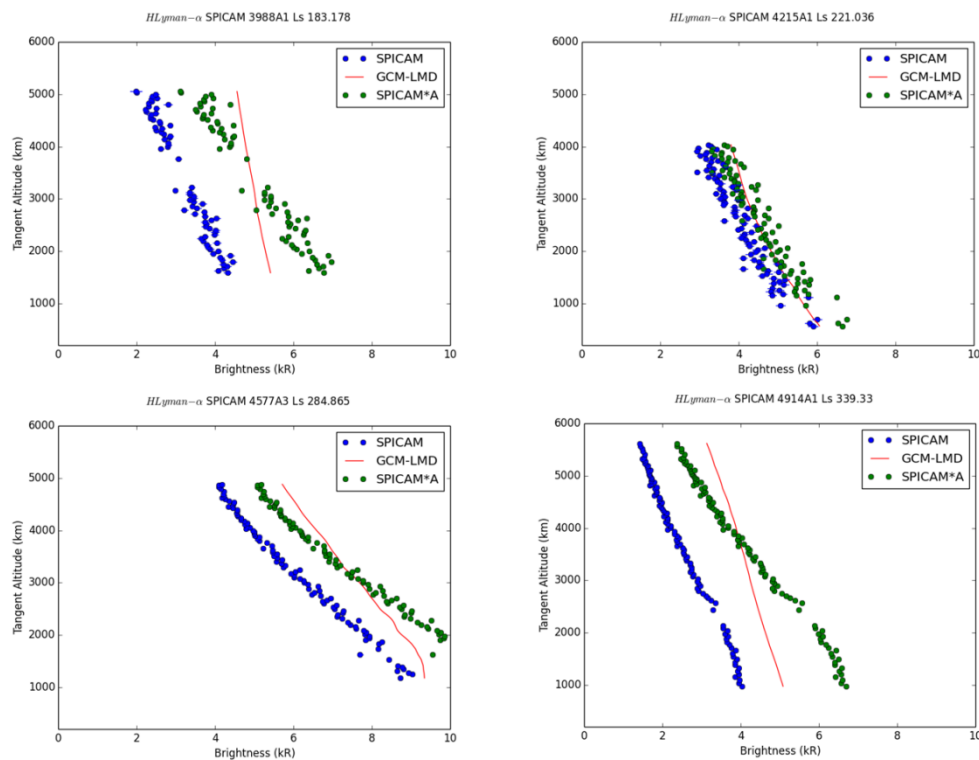
334 thermosphere, [while Shaposhnikov et al. \(2019\) suggest, using a GCM, that a “pump” mechanism could facilitate](#)
 335 [upward transport at high latitude during perihelion](#). Seasonal variations of the altitude of the hygropause at Mars are
 336 present in the LMD-GCM simulations (Montmessin et al. 2005). Fig. 9 displays a typical density profile for H, H₂,
 337 H₂O, and CO₂ and the temperature profile obtained for Martian year 28 at the equator at noon for the month Ls =
 338 120-150 and Ls = 270° - 300°. At Ls = 120-150°, the water vapor is confined to very low altitudes (< 20 km). The
 339 hydrogen density presents a double-peaked profile, one peak in the low atmosphere due to water vapor
 340 photodissociation, and another peak in the low thermosphere due to ionospheric reactions (Krasnopolsky 2002). At
 341 Ls=240-270°, the hygropause is ~ 50 km, but there are still substantial amounts of water vapor in the mesosphere
 342 near 80 km but not above 120 km. Only one hydrogen density peak is observed, because the peak associated with
 343 ionospheric reactions is merged with the hydrogen coming from water photodissociation transported from the lower
 344 atmosphere which is ~100 times larger.



345
 346 *Fig. 9 Vertical density profile of the main hydrogen species and CO₂ at noon equator from the surface to the exobase*
 347 *simulated for two different months during the Martian year 28.*

348
 349 The dissociation of water vapor is a source of atomic hydrogen in the Martian lower thermosphere. Such an effect

350 could be the main driver of our simulated escape rate, contrary to our first interpretation (Chaufray et al. 2015a). This
 351 would partly explain the difference between our simulations and the model of Krasnopolsky (2002), as suggested by
 352 Krasnopolsky (2017). An increase in the water vapor density could explain the current underestimate of the hydrogen
 353 escape at $L_s = 270^\circ$ - 300° , and would be in agreement with the conclusion of Maltagliati et al. (2013), who found that
 354 the GCM-LMD underestimates the water vapor in the Martian mesosphere at this season, since the description of the
 355 water cycle presented in this study is done with similar assumptions than those used by these authors. This
 356 discrepancy was attributed to an underestimation of the strength of the interaction between the water vapor and the
 357 dust cycles. The water vapor mixing ratio in the mesosphere depends on the supersaturation of the upper atmosphere,
 358 which is not well known. The microphysical processes controlling supersaturation are now included in the LMD-
 359 GCM (Navarro et al. 2014), but their effects on the water vapor at high altitudes depends on model parameters not
 360 well constrained by the observations and therefore were not included in these simulations. A similar comparison with
 361 the few SPICAM observations displayed in Fig. 4 of the simulations used to generate the Mars Climate Database 5.2
 362 (for the Martian year 28), including these microphysical processes is displayed in Fig. 10



363
 364
 365 *Fig. 10 Same as Fig. 4 but for the simulations used to generate the MCD 5.2, including the microphysical processes*
 366 *controlling the supersaturation.*

367 In these simulations, the Lyman-alpha brightness is overestimated, even at the southern summer. The brightness

368 profiles for observations 4215A1 is in good agreement, while the simulated shape profiles of the three other
369 observations is very different from the observed shape suggesting that the difference is due to an overestimate of the
370 hydrogen density in the Martian upper altitude. The average hydrogen escape rate for $L_s = 270\text{-}300^\circ$ used to simulate
371 the observation 4501 is $1.1 \times 10^{27} \text{ s}^{-1}$, larger by ~ 2 compared with the escape rate estimated in section 4 after a global
372 rescale of the hydrogen density. Although not perfect, the updated LMD-GCM microphysical processes could be
373 sufficient to produce the large amount of hydrogen lacking in our previous simulations. Our simulations could also be
374 consistent with the ionospheric observations by MAVEN/NGIMS, because if the amount of water vapor coming from
375 the lower atmosphere is larger at 120 km, but remains negligible above 150 km, it could prevent the HCO^+
376 destruction while producing H_3O^+ ions near 120 km (Fox et al. 2015). A more detailed study of the link between the
377 water vapor and the atomic hydrogen and ionospheric water species will benefit from future observations of the water
378 vapor density in the Martian mesosphere/thermosphere by Exo Mars Trace Gas Orbiter (Lopez-Valverde et al. 2018),
379 especially during the recent global dust storm in June 2018. Comparisons of other Martian years like Martian year 32
380 where an increase of water vapor was also observed by SPICAM (Fedorova et al. 2018), and using the large Lyman- α
381 dataset of MAVEN/IUVS (Chaffin et al. 2015, 2018) will be also useful to estimate the year to year variability
382 possibly due to dust events and the variability associated with the solar activity in order to extrapolate past conditions
383 with larger EUV solar flux and orbit parameters. Space weather events also increase the atmospheric escape rates
384 (Jakosky et al. 2015). But they mostly increase the heavy ions escape rates as reported in Jakosky et al. (2015)
385 during the interplanetary coronal mass ejection in March 2015. Solar flares could heat the Martian upper atmosphere
386 and increase the escape rate during short time periods (Mayyasi et al. 2018).

387 Considering the discrepancy of our model and the SPICAM observations, we estimated the hydrogen escape rate
388 during these two Martian years to vary between $\sim 10^{25}$ to $6 \times 10^{26} \text{ s}^{-1}$. This range is in good agreement with the
389 seasonal variations ($3 \times 10^{25} \text{ s}^{-1}$ near aphelion and $4 \times 10^{26} \text{ s}^{-1}$ near perihelion) reported from pick-up protons for the
390 Martian years 32-33 by Rahmati et al. (2018), and from Lyman- α emission by Chaffin et al. (2018) (estimated $\sim 5\text{-}$
391 $14 \times 10^{26} \text{ s}^{-1}$ at $L_s = 250^\circ$ for MY 32 and $1\text{-}4 \times 10^{26} \text{ s}^{-1}$ at $L_s = 200^\circ$ for MY 33). It is slightly lower than the escape rate
392 estimated from the hydrogen column upstream of the bow shock by Halekas (2017); considering $T = 200 \text{ K}$ near
393 aphelion, and $T=300 \text{ K}$ near perihelion, and assuming an uniform escape rate, the escape flux derived from Fig. 5 of
394 Halekas (2017) leads to an escape rate variation from $\sim 3 \times 10^{25}$ to $\sim 3 \times 10^{27} \text{ s}^{-1}$. If we express this escape flux into a
395 water Global Equivalent Layer (GEL) d using

396
$$d(m / Gyr) = \frac{\Phi_H}{2} \frac{m_{H_2O}}{\rho_{H_2O} S} T,$$

397 where $\Phi_H/2$ is the water loss rates, m_{H_2O} the mass of a water molecule, ρ_{H_2O} water mass density, S the Martian surface
398 and T the number of seconds in 1 Gyr ($\sim 3.2 \times 10^{16}$ s/Gyr), we find a loss between ~ 33 to 2000 mm per billion years
399 and therefore no more than 10 m GEL during the last 4 billion years, which is small compared to the total water
400 content measured in the reservoirs at the surface and the subsurface (~ 30 m), and even less compared to the
401 estimated amount of water needed to form the valley networks or outflow channels (estimated to few 100s m GEL
402 with large uncertainties, Lasue et al. 2013). The differences could be either due to a more important hydrogen escape
403 rate in the past or to a larger reservoir of water (ice or liquid) in the subsurface inaccessible or not yet detected by
404 current radar (Orosei et al. 2015, 2018).

405 **6) Conclusion**

406 We simulated the atomic hydrogen content in the upper atmosphere of Mars for Martian years 28 and 29. These two
407 years correspond to a period of numerous hydrogen coronal observations by SPICAM on Mars Express. The
408 comparison between our simulated brightness and SPICAM observations shows a reasonable agreement with the
409 observations for $L_s < 200^\circ$ and $L_s > 330^\circ$ for Martian year 28, for $L_s < 150^\circ$ and $L_s > 340^\circ$ for Martian year 29, while
410 the simulated brightness is strongly underestimated for $230 < L_s < 330^\circ$ for Martian year 28 and $270^\circ < L_s < 340^\circ$ for
411 Martian year 29 (therefore, around and after the southern solstice equinox at $L_s=270^\circ$ and the perihelion crossing at
412 $L_s=251^\circ$). This underestimate corresponds to a model underestimate of the global hydrogen density (and the Jeans
413 escape rate) by a factor ~ 6 . Therefore, our study confirms that the seasonal variations of the hydrogen escape at Mars
414 could be of almost two orders of magnitude, as suggested by Chaffin et al. (2014). It also confirms that this variation
415 is a seasonal variation which may be expected every Martian year, as observed from plasma measurements by Mars
416 Express (Yamauchi et al. 2015) and more recently by MAVEN for the Martian year 32, and 33 (e.g., Clarke et al.
417 2017, Halekas 2017, Rahmati et al. 2018, Chaffin et al. 2018). The discrepancy between our simulations and the
418 observations is attributed to an LMD-GCM underestimate of the amount of water vapor transported to high
419 altitudes. Accurate observations of the water vapor density in the Martian upper atmosphere by TGO ([Vandaele et
420 al. 2019](#)) or MAVEN/NGIMS could help to better the understanding of the details of this transport.

422 **Acknowledgements**

423

424
 425 This project was partially funded by the Programme National de Planetologie and Programme National Soleil Terre
 426 and by the Centre National d'Etudes Spatiales. This work has been partially funded by the European Union Horizon
 427 2020 Programme (H2020 Compet -08-2014) under grant agreement UPWARDS-633127. We would like to thank G.
 428 Lacombe and L. Baggio for their support on the calibration. We thank Allyson Leffler for her careful review of
 429 grammatical aspects of this paper. The SPICAM/MEX data used in this study are available through the ESA
 430 Planetary Science Archive (PSA, <https://archives.esac.esa.int/psa/>). The monthly average 3D simulated hydrogen
 431 exosphere can be found on : <https://owncloud.latmos.ipsl.fr/index.php/s/AdUgv9PdipA2rim>

432
 433 **Appendix : List of SPICAM-UV observations used in this study.**
 434

435 The list of the SPICAM observations used for the Martian year 28 and 29, and some geometric parameters are given
 436 in Table 1 and Table 2 respectively

437

Orbit and Sequence	Date	Ls	Altitude range (km)	SZA range	Latitude range	Slit/No slit	Binning/Y ₀	Band used
3668A1	15 Nov 2006	135.4	600 - 5600	56°	32S	Slit	32/22	5
3838A2	02 Jan 2007	159.8	500- 5500	57°	7N	Slit	32/22	5
3896A1	18 Jan 2007	168.4	600 - 5600	66°	5N	Slit	32/22	5
3988A1	13 Feb 2007	182.9	600-5000	79°	23S	Slit	32/22	5
3989A1	13 Feb 2007	182.9	500 - 4500	79°	37S	Slit	32/22	5
4001A1	17 Feb 2007	185.1	500 - 4800	80°	26S	Slit	32/22	5
4085A1	12 Mar 2007	198.6	1000-4300	39-67	1S – 18S	Slit	32/22	5
4114A1	20 Mar 2007	203.3	900-4600	40-73	12S – 32S	Slit	32/22	5
4178A1	07 Apr 2007	214.3	800 - 4500	50-86	3S – 28S	Slit	32/22	5
4192A1	11 Apr 2007	216.7	500-4100	50-88	4N – 24S	Slit	32/22	5
4215A1	17 Apr 2007	220.4	500-4100	55-93	7N – 22S	Slit	32/22	5
4219A1	18 Apr 2007	221.0	400-3600	57-92	19N – 13S	Slit	32/22	5
4407A4	10 Jun 2007	254.4	500-4000	10-80	14S – 54N	Slit	32/118	4
4475A1	29 Jun 2007	266.5	400 -4200	36-86	4S – 58N	Slit	32/118	4
4501A1	07 Jul 2007	271.5	900 - 4300	14-67	14S – 44N	No Slit	32/118	1

4577A3	28 Jul 2007	284.6	1100-4800	8 -60	16S – 34N	Slit	32/118	4
4646A1	16 Aug 2007	296.2	1300-5600	58	28N	Slit	32/118	4
4671A2	23 Aug 2007	300.4	1100-5100	47°	10N	No Slit	32/118	1
4673A2	24 Aug 2007	301.0	1300-5500	51°	17N	Slit	32/118	4
4693A2	29 Aug 2007	304.0	300 -10000	36-96	5N – 76N	Slit	32/118	4
4729A1	08 Sep 2007	309.8	1100-3500	45°	23S	No slit	32/118	1
4740A1	11 Sep 2007	311.6	1100 - 3600	47°	25S	Slit	32/118	4
4757A2	16 Sep 2007	314.5	700 - 3600	50°	28S	No slit	32/118	1
4769A2	20 Sep 2007	316.8	300-10000	19-85	1S - 63N	Slit	32/118	4
4772A2	20 Sep 2007	316.8	700 – 3600	53	31S	Slit	32/118	4
4785A1	24 Sep 2007	319.1	700 – 3600	56	33S	Slit	32/118	4
4794A2	27 Sep 2007	320.8	800 - 10000	19 - 90	2N – 60N	Slit	32/118	4
4796A1	27 Sep 2007	320.8	700 - 3600	57	34S	No Slit	32/118	1
4856A1	14 Oct 2007	330.2	700 – 3600	69	45S	No Slit	32/118	1
4903A1	27 Oct 2007	337.3	1400-5500	76	23S	No Slit	32/118	1
4905A1	28 Oct 2007	337.8	700 - 5600	77	10S	Slit	32/118	4
4910A1	29 Oct 2007	338.4	1000-5600	77	17S	No Slit	32/118	1
4914A1	30 Oct 2007	338.9	1000-5600	78	18S	Slit	32/118	4
4923A1	02 Nov 2007	340.5	700-5000	79	34S	No Slit	32/118	1
4950A1	09 Nov 2007	344.2	700-5000	84	39S	Slit	32/118	4
5005A1a	25 Nov 2007	352.5	300-3300	32-56	24S – 9N	Slit	32/118	4
5016A1	28 Nov 2007	354.0	600-3600	35-59	14S – 14N	Slit	32/118	4
5024A1	30 Nov 2007	355.1	500-3700	34-61	17N – 29N	Slit	32/118	4
5052A1	08 Dec 2007	359.1	500-3900	36-66	18N – 31N	Slit	32/118	4

438 *Table 1 : List of SPICAM-UV observations used to study the Martian hydrogen corona during the Martian year 28.*
439 *The orbit number and sequence number of the observations are given in column 1. Column 3 gives the approximate*
440 *solar longitude Ls at the observation day. Columns 4 and 5 refer to the tangent point of the line of sight.*

441
442

Orbit and Sequence	Date	Ls	Altitude range	SZA range	Latitude range	Slit/No slit	Binning/Y	Band used
5070A1	13 Dec 2007	1.6	800-4300	41-70	15N – 29N	Slit	32/118	4
5097A1	21 Dec 2007	5.5	900-10,000	75-107	0 – 60N	Slit	32/118	4
5119A1	27 Dec 2007	8.5	1000-4800	50-80	16N – 32N	Slit	32/118	4

5122A1	28 Dec 2007	8.9	1000-4500	50-80	7N – 25N	No Slit	32/118	1
5129A1	30 Dec 2007	9.9	900-4400	50-80	4N – 22N	Slit	32/118	4
5135A1	31 Dec 2007	10.4	900-4600	50-82	14N – 33N	Slit	32/118	4
5154A1	06 Jan 2008	13.3	950-4500	55-85	0 – 20N	Slit	32/118	4
5156A1	06 Jan 2008	13.3	1100-4900	56-87	13N – 32N	Slit	32/118	4
5266A1	07 Feb 2008	28.3	450-4300	40-99	23S – 85S	Slit	32/118	4
5283A1	12 Feb 2008	30.6	700-4500	48-99	34S – 71S	No Slit	32/118	1
5290A2	14 Feb 2008	31.5	700-4500	48-99	34S – 72S	Slit	32/118	4
5304A1	18 Feb 2008	33.3	600-4400	40-97	22S – 83S	No Slit	32/118	1
5341A1	28 Feb 2008	37.9	600-4400	35-95	19S – 78S	Slit	32/118	4
5353A1	03 Mar 2008	39.7	500-4300	31-92	14S – 76S	No Slit	32/118	1
5367A1	07 Mar 2008	41.5	500-4400	33-93	16S – 75S	Slit	32/118	4
5374A1	09 Mar 2008	42.4	500-4300	30-92	12S – 73S	No Slit	32/118	1
5388A1	13 Mar 2008	44.2	600-4000	52-101	29S – 59S	Slit	32/118	4
5390A1	13 Mar 2008	44.2	600-4000	52-101	28S – 59S	No Slit	32/118	1
5404A1	17 Mar 2008	45.9	600-4000	50-100	26S – 62S	Slit	32/118	4
5416A1	21 Mar 2008	47.7	600-4100	47-98	22S – 64S	No Slit	32/118	1
5432A1	25 Mar 2008	49.5	600-4100	46-98	21S – 65S	Slit	32/118	4
5446A1	29 Mar 2008	51.3	600-4200	43-95	17S – 66S	No Slit	32/118	1
5462A1	03 Apr 2008	53.5	600-4000	51-100	21S – 63S	Slit	32/118	4
5546A1	27 Apr 2008	64.0	400-3600	57-100	12S – 59S	Slit	32/118	4
5617A2	17 May 2008	72.7	500-4000	40-77	14N – 43S	Slit	32/118	4
5662A2	30 May 2008	78.4	400-3900	35-70	17N – 39S	Slit	32/118	4
5715A2	14 Jun 2008	85.0	800-3400	60-91	12S – 46S	No Slit	32/118	1
5726A2	17 Jun 2008	86.3	900-3300	58-89	11S – 45S	No Slit	32/118	1
5759A2	26 Jun 2008	90.7	300-1900	30-70	23N – 31S	Slit	32/118	4
6168A1*	21 Oct 2008	144.9	730-200-1200	105-48-49	52S – 61N	Slit	32/23	5
6200A1*	30 Oct 2008	149.4	900-200-1300	101-51-55	64S – 61N	Slit	32/23	5
6206A1*	01 Nov 2008	150.5	1200-200-1300	95-59-64	73S – 60N	Slit	32/23	5
6213A1*	03 Nov 2008	151.5	900-200-1300	100-50-55	66S – 60N	Slit	32/23	5
6440A1	07 Jan 2009	187.0	900-110-1200	87-72-78	73S – 23N	Slit	32/118	4
6478A1*	18 Jan 2009	193.3	1200-200-600	100-46-49	23S-61S-16S	Slit	32/118	4

6521A1	30 Jan 2009	200.6	1300-100-1200	130-35	40S-73S-2S	Slit	32/118	4
6546A1*	06 Feb 2009	204.9	1300-200-1100	120-28	27S-65S-13S	Slit	32/118	4
6593A1*	20 Feb 2009	213.1	1100-200-500	120-44	3S-72S-42S	Slit	32/118	4
6666A1	13 Mar 2009	226.1	1300-100-1300	140-12	19S-74S-23S	Slit	32/118	4
6691A3*	20 Mar 2009	230.4	1300-200-1300	140-13	14S-66S-26S	Slit	32/118	4
6722A1*	29 Mar 2009	236.2	1300-200-1300	150-20	9S-67S-31S	Slit	32/118	4
6765A1	10 Apr 2009	244.1	900-100-1200	135-10	18S-70S-24S	Slit	32/118	4
6801A1	20 Apr 2009	250.0	1300-100-1200	140-35	7N-77S-27S	Slit	32/118	4
6832A1	29 Apr 2009	256.3	800-100-1200	140-10	9S-66S-32S	Slit	32/118	4
6859A1	07 May 2009	261.2	900-90-1200	140-15	2S-66S-39S	Slit	32/118	4
6888A1	15 May 2009	266.5	900-90-1200	140-20	3N-65S-43S	Slit	32/118	4
6895A1	17 May 2009	267.7	900-90-1200	140-20	4N-65S-44S	Slit	32/118	4
6949A1	02 Jun 2009	277.5	1300-10-900	150-65	42N – 87S	Slit	32/118	4
6956A2	04 Jun 2009	278.4	1300-10-900	150-65	43N – 87S	Slit	32/118	4
6960A1	05 Jun 2009	279.	1300-10-800	144-74	41N – 81S	Slit	32/118	4
6967A1	07 Jun 2009	280.3	1300-10-800	145-75	42N – 80S	Slit	32/118	4
7045A2&3	29 Jun 2009	294.	3300-8500-7700	64-84	19S – 14S	Slit	32/118	4
7046A1&2 ⁺	30 Jun 2009							
7089A3&4	12 Jul 2009	301.6	2900-9200-8800	70-89	20S – 14S	Slit	32/118	4
7090A1&2	12 Jul 2009							
7122A2&3	22 Jul 2009	307.5	2400-9600-9300	73-94	21S – 15S	Slit	32/118	4
7123A1&2	22 Jul 2009							
7292A1	08 Sep 2009	334.6	2500-4000	53-58	58S – 40S	Slit	32/118	4
7293A1	09 Sep 2009	335.2	2800-4300	54-59	57S – 39S	Slit	32/118	4
7320A2	17 Sep 2009	339.5	2100-4100	56-63	67S – 52S	Slit	32/118	4
7321A2	17 Sep 2009	339.5	2400-4300	57-63	67S – 52S	Slit	32/118	4
7421A1	16 Oct 2009	354.6	4200-5600	78	74S	Slit	32/118	4
7423A1	16 Oct 2009	354.6	200-3000	76	76S	Slit	32/118	4
7446A1	23 Oct 2009	358.1	4400-6200	81	73S	Slit	32/118	4
7447A3	23 Oct 2009	358.1	4500-6300	80	73S	Slit	32/118	4

443 *Table 2 : List of SPICAM-UV observations used to study the Martian hydrogen corona during the Martian year 29.*
444 *The orbit number and sequence number of the observations are given in column 1. Column 3 gives the approximate*
445 *solar longitude Ls at the observation day. Columns 4, 5 and 6 refer to the tangent point of the line of sight. *For*
446 *these observations solar scattered light is observed at low altitudes on all bands polluting the airglow emissions.*

447 *Only altitudes above ~200 km are considered in these cases.*

448
449
450
451
452
453
454
455
456
457
458
459
460
461
462
463
464
465

466

467 **References**

468

469 Bertaux, J-L., O. Korablev, S. Perrier, E. Quémerais, F. Montmessin, F. Leblanc, S. Lebonnois, P. Rannou, F.

470 Lefevre, F. Forget, A. Fedorova, E. Dimarellis, A. Reberac, D. Fonteyn, J-Y. Chaufray, and S. Guibert,

471 SPICAM on Mars Express : Observing modes and overview of UV spectrometer data and scientific results, J.

472 Geophys. Res., 111, E10S90, doi:10.1029/2006JE002690, 2006

473 Bertucci, C., N. Romanelli, J-Y. Chaufray, D. Gomez, C. Mazelle, M. Delva, R. Modolo, F. Gonzalez-Galindo, and

474 D.A. Brain, Temporal variability of waves at the proton cyclotron frequency upstream from Mars :

475 Implication for Mars distant hydrogen exosphere, Geophys. Res. Lett., 40, 3809-3813, doi:10.1002/grl.50709,

476 2013

477 Beth, A., P. Garnier, D. Toublanc, I. Dandouras, and C. Mazelle, (2016), Theory for planetary exospheres : II

478 Radiation pressure effect on exospheric density profiles, Icarus, 266, 423- 432

479 Bhattacharyya, D., J.T. Clarke, J-L. Bertaux, J-Y. Chaufray, M.Mayyasi, (2015), A strong seasonal dependence in the

480 martian hydrogen exosphere, Geophys. Res. Lett., 42, 8678- 868

481 Bhattacharyya, D., J.T. Clarke, J-L. Bertaux, J-Y. Chaufray, and M. Mayyasi, (2017) Analysis and modeling of

482 remote observations of the martian hydrogen exosphere, Icarus, 281, 264-280

483 Bibring, J-P., Y. Langevin, J. Mustard, F. Poulet, R. Arvidson, A. Gendrin, B. Gondet, N. Mangold, P. Pinet, F.

484 Forget, and the OMEGA team, Global Mineralogical and Aqueous history of Mars derived from

485 OMEGA/Mars Express data, *Science*, 312, 400-404, (2006)

486 Bishop, J., et al., Phyllosilicate diversity and past aqueous activity revealed at Mawrth Vallis, Mars, *Science*, 321,
487 830-833, doi : 10.1126/science.1159699, (2008)

488 Boqueho, V., and P-L. Blelly, Contributions of a multimoment multispecies approach in modeling planetary
489 atmospheres: Example of Mars, *J. Geophys. Res.*, 110, A01313, doi: 10.1029/2004JA010414, 2005

490 Brinkmann, R.T., Departures from Jeans' escape rate for H and He in the Earth's atmosphere, (1970), *Planet. Space*
491 *Sci.*, 18, 449-478

492 Chaffin, M.S., J-Y. Chaufray, I.A.F Stewart, F. Montmessin, N.M. Schneider, and J-L. Bertaux, (2014), Unexpected
493 variability of Martian hydrogen escape, *Geophys. Res. Lett.*, 41, 314- 320, doi: 10.1002/2013GL058578

494 Chaffin, M.S., J. Deighan, N.M. Schneider, and A.I.F. Stewart, Elevated atmospheric escape of atomic hydrogen
495 from Mars induced by high-altitude water, *Nat. Geosc.*, 10, 174-178, (2017)

496 Chaffin, M.S., J-Y. Chaufray, J. Deighan, N.M. Schneider, M. Mayyasi, J.T. Clarke, E. Thiemann, S.K. Jain, M.M.J.
497 Crismani, A. Stiepen, F.G. Eparvier, W.E. McClintock, A.I.F. Stewart, G.M. Holsclaw, F. Montmessin, and
498 B.M. Jakosky, Mars H escape rates derived from MAVEN/IUVS Lyman- α brightness measurements and their
499 dependence on model assumptions, *J. Geophys. Res: Planets*, 123, 2192-2210, doi: 10.1029/2018JE005574,
500 (2018)

501 Chaufray, J-Y., J-L. Bertaux, F. Leblanc, and E. Quémerais, (2008), Observation of the hydrogen corona with
502 SPICAM on Mars Express, *Icarus*, 195, 598-613

503 Chaufray, J-Y., F. Leblanc, E. Quémerais, and J-L. Bertaux, Martian oxygen density at the exobase deduced from OI
504 130.4 nm observations by SPICAM on Mars Express, *J. Geophys. Res.*, 114, E02006,
505 doi:10.1029/2008JE003130, 2009

506 Chaufray, J-Y., J-L. Bertaux, E. Quémerais, E. Villard, F. Leblanc, Hydrogen density in the dayside venusian
507 exosphere derived from Lyman- α observations by SPICAV on Venus Express, *Icarus*, 217, 767-778, 2012

508 Chaufray, J-Y., F. Gonzalez-Galindo, F. Forget, M.A. Lopez-Valverde, F. Leblanc, R. Modolo, and S. Hess, (2015a),
509 Variability of the hydrogen in the martian upper atmosphere as simulated by a 3D atmosphere-exosphere
510 coupling, *Icarus*, 245, 282-294

511 Chaufray, J-Y., J-L. Bertaux, F. Leblanc, E. Quémerais, and S. Sulis, (2015b), Observations of the nightside venusian
512 hydrogen corona with SPICAV/VEX, *Icarus*, 262, 1-8

513 Chaufray, J-Y., F. Gonzalez-Galindo, F. Forget, M.A. Lopez-Valverde, F. Leblanc, R. Modolo, and S. Hess, (2017),
514 Reply to comment « On the hydrogen escape: Comment to Variability of the hydrogen in the Martian upper
515 atmosphere as simulated by a 3D atmosphere-exosphere coupling by J-Y Chaufray et al.” by V.
516 Krasnopolsky, *Icarus*, 281, 262, doi : 10.1016/j.icarus.2017.07.013

517 Chaufray, J-Y., R.V. Yelle, F. Gonzalez-Galindo, F. Forget, M. Lopez-Valverde, F. Leblanc, R. Modolo, (2018),
518 Effect of the lateral exospheric transport on the horizontal hydrogen distribution at the exobase of Mars, *J.*
519 *Geophys. Res.*, 123, 4241-4254, doi : 10.1002/2017JA025163

520 Clancy, R.T., B.J. Sandor, M.J. Wolff, P.R. Christensen, M.D. Smith, J.C. Pearl, B.J. Conrath, and R.J. Wilson, An
521 intercomparison of ground-based millimeter, MGS TES, and Viking atmospheric temperature measurements:
522 Seasonal and interannual variability of temperatures and dust loading in the global Mars atmosphere, *J.*
523 *Geophys. Res.*, 105, 9553-9571, 2000

524 Clarke, J. T., J-L. Bertaux, J-Y. Chaufray, G.R. Gladstone, E. Quémerais, J.K. Wilson, and D. Bhattacharyya, A rapid
525 decrease of the hydrogen corona of Mars, *Geophys. Res. Lett.*, 41, 8013-8020, 2014

526 Clarke, J.T., M. Mayyasi, D. Bhattacharyya, N.M. Schneider, W.E. McClintock, J.I. Deighan, A.I.F. Stewart, J-Y.
527 Chaufray, M.S. Chaffin, S.K. Jain, A. Stiepen, M. Crismani, G.M. Holsclaw, F. Montmessin, and B. Jakosky,
528 Variability of D and H in the Martian upper atmosphere observed with the MAVEN IUVS echelle channel, *J.*
529 *Geophys. Res.*, 122, 2336-2344, doi: 10.1002/2016JA023479

530 Emerich, C., P. Lemaire, J-C. Vial, W. Curdt, U. Schüle, K. Wilhelm, A new relation between the central spectral
531 solar H I Lyman α irradiance and the line irradiance measured by SUMER/SOHO during the cycle 23., *Icarus*,
532 178, 429-433, (2005)

533 Fedorova, A., J-L. Bertaux, D.Betsis, F. Montmessin, O. Korablev, L. Maltagliati, and J. Clarke, Water vapor in the
534 middle atmosphere of Mars during the 2007 global dust storm, *Icarus*, 300, 440, 2018

535 Forget, F., F. Hourdin, R. Fournier, C. Hourdin, O. Talagrand, M. Collins, S.R. Lewis, P.L. Read, J-P. Huot,
536 Improved general circulation models of the Martian atmosphere from the surface to above 80 km, *J. Geophys.*
537 *Res.*, 104, 24,155-24,175, 1999

538 Fox J.L., M. Benna, P.R. Mahaffy, and B.M. Jakosky, Water and water ions in the Martian thermosphere/ionosphere,
539 *Geophys. Res. Lett.*, 42, 8977-8985, doi: 10.1002/2015GL065465, (2015)

540 Gladstone, G.R., Auroral resonance line radiative transfer, *J. Geophys. Res.*, 97, 1377-1387, 1992

541 Gonzalez-Galindo, F., F. Forget, M.A. Lopez-Valverde, M. Angelats i Coll, and E. Millour, A ground-to-exosphere
542 Martian general circulation model: 1 Seasonal, diurnal, and solar cycle variation of thermospheric
543 temperatures, *J. Geophys. Res.*, 114, E04001, doi:10.1029/2008JE003246, 2009

544 Gonzalez-Galindo, F., M.A. Lopez-Valverde, F. Forget, M. Garcia-Comas, E. Millour, and L. Montabone, (2015),
545 Variability of the Martian thermosphere during eight Martian years as simulated by a ground-to-exosphere
546 global circulation model, *J. Geophys. Res.*, 120, 2020-2035, doi:10.1002/2015JE004925

547 Halekas, J. S. (2017), Seasonal variability of the hydrogen exosphere of Mars, *J. Geophys. Res. Planets*, 122,
548 doi:10.1002/2017JE005306

549 Heavens et al, Hydrogen escape from Mars enhanced by deep convection in dust storms, *Nature Astronom*, 2, 126–
550 132 (2018)

551 Hynek, B.M., M. Beach, and M.R.T. Hoke, Updated global map of Martian valley networks and implications for
552 climate and hydrologic processes, *J. Geophys. Res.*, 115, E09008, doi: 10.1029/2009JE003548, (2010)

553 Jakosky, B. et al., Loss of the Martian atmosphere to space: Present-day loss rates determined from MAVEN
554 observations and integrated loss through time, *Icarus*, 315, 146-157, (2018)

555 Krasnopolsky, V., Mars' upper atmosphere and ionosphere at low, medium, and high solar activities: Implications for
556 evolution of water, *J. Geophys. Res.*, 107(E12), 5128, doi: 10.1029/2001JE001809, 2002

557 [Krasnopolsky, V., Solar activity variations of thermospheric temperatures on Mars and a problem of CO in the lower](#)
558 [atmosphere, *Icarus*, 207, 638-647, \(2010\)](#)

559 Krasnopolsky, V., On the hydrogen escape from Mars: comments to “Variability of the hydrogen in the Martian
560 upper atmosphere as simulated by a 3D atmosphere-exosphere coupling” by JY Chaufray et al., *Icarus*, 281,
561 262-263, (2017)

562 [Krasnopolsky, V.A., Photochemistry of water in the martian thermosphere and its effect on hydrogen escape, *Icarus*,](#)
563 [321, 62-70, 2019](#)

564 Lasue, J., N. Mangold, E. Hauber, S. Clifford, W. Feldman, O. Gasnault, C. Grima, S. Maurice, and O. Mousis,
565 Quantitative assessments of the Martian hydrosphere, *Space Sci. Rev.*, 174, 155-212, (2013)

566 Leblanc, F., J-Y. Chaufray, J. Lilensten, O. Witasse, and J-L. Bertaux, Martian dayglow as seen by the SPICAM UV
567 spectrograph on Mars Express, *J. Geophys. Res.*, 111, E09S11, doi: 10.1029/2005JE002664, 2006

568 Lee, J.S., Refined Monte Carlo method for simulating angle-dependent partial frequency redistributions, *Astrophys.*

569 J., 255, 303-306, 1982

570 Lopez-Valverde, M.A. et al., Investigation of the Mars upper atmosphere with ExoMars Trace Gas Orbiter, Space
571 Sci. Rev., 214:29, doi: 10.1007/s11214-017-0463-4, (2018)

572 Maltagliati, L., F. Montmessin, O. Korablev, A. Fedorova, F. Forget, A. Määttänen, F. Lefèvre, and J-L. Bertaux,
573 (2013) Annual survey of water vapor vertical distribution and water- aerosol coupling in the martian
574 atmosphere observed by SPICAM/Mex solar occultations, *Icarus*, 223, 942-962

575 Mayyasi, M., D. Bhattacharyya, J. Clarke, A. Catalano, M. Benna, P. Mahaffy, E. Thiemann, C. Lee, J. Deighan, J.
576 Sonal, and 9 co-authors, (2018), Significant space weather impact on the escape of hydrogen from Mars,
577 *Geophys. Res. Lett.*, 45, 8844

578 Montabone, L., F. Forget, E. Millour, R.J. Wilson, S.R. Lewis, B. Cantor, D. Kass, A. Kleinbohl, M.T. Lemmon,
579 M.D. Smith, M.J. Wolff, Eight-year climatology of dust optical depth on Mars, *Icarus*, 251, 65-95, 2015

580 Montmessin, F., F. Forget, P. Rannou, M. Cabane, R. M. Haberle, Origin and role of water ice clouds in the Martian
581 water cycle as inferred from a general circulation model, *J. Geophys. Res.*, 109, E10004, doi :
582 10.1029/2004JE002284, 2004

583 Montmessin, F., O. Korablev, F. Lefevre, J-L. Bertaux, A. Fedorova, A. Trokhimovskiy, J-Y. Chaufray, G. Lacombe,
584 A. Reberac, L. Maltagliati, Y. Willame, S. Guslyakova, J-C. Gerard, A. Stiepen, D. Fussen, N. Mateshvili, A.
585 Maatanen, F. Forget, O. Witasse, F. Leblanc, A.C. Vandaele, E. Marcq, B. Sandel, B. Gonder, N. Schneider,
586 M Chaffin, N. Chapron, SPICAM on Mars Express: A 10 year in-depth survey of the Martian atmosphere,
587 *Icarus*, 297, 195-216, 2017

588 Navarro, T., J.-B. Madeleine, F. Forget, A. Spiga, E. Millour, F. Montmessin, and A. Määttänen. Global climate
589 modeling of the Martian water cycle with improved microphysics and radiatively active water ice clouds.
590 *Journal of Geophysical Research (Planets)*, 119:1479- 1495, 2014

591 Orosei, R., R.L. Jordan, D.D Morgan, M. Cartacci, A. Cicchetti, F. Duru, D.A. Gurnett, E. Heggy, D.L. Kirchner, R.
592 Noschese, W. Kofman, A. Masdea, J-J. Plaut, R. Seu, T.R. Watters, G. Picardi, Mars Advanced Radar for
593 subsurface and ionospheric sounding (MARSIS) after nine years of operation : A summary, *Planet Space Sci.*,
594 112, 98-114, (2015)

595 Orosei, R., S.E. Lauro, E. Pettinelli, A. Cicchetti, M. Coradini, B. Cosciotti, F. Di Paolo, E. Flamini, E. Mattei, M.
596 Pajola, and 12 co-authors, Radar evidence of subglacial liquid water on Mars, *Science*, 361, 490, (2018)

597 Quémerais, E., Angle dependent partial frequency redistribution in the interplanetary medium at Lyman- α , *Astron.*
598 *Astrophys.*, 358, 353-367, 2000

599 Rahmati, A., D.E. Larson, T.E. Cravens, R.J. Lillis, J.S. Halekas, J.P. McFadden, D.L. Mitchell, E.M.B. Thiemann,
600 J.E.P. Connerney, P.A. Dunn, C.O. Lee, F.G. Eparvier, G.A. DiBraccio, J.R. Espley, J.G. Luhmann, C.
601 Mazelle, and B.M. Jakosky, Seasonal variability of neutral escape from Mars as derived from MAVEN
602 pickup ion observations, *J. Geophys. Res. : Planets*, 123, 1192-1202, 10.1029/2018JE005560, (2018)

603 Romanelli, N. C. Mazelle, J-Y. Chaufray, K. Meziane, L. Shan, S. Ruhunusiri, J.E.P. Connerney, J. R. Espley, F.
604 Eparvier, T.E. Thiemann, et al., 2016, Proton cyclotron, waves occurrence rate upstream from Mars observed
605 by MAVEN : Associated variability of the Martian upper atmosphere, *J. Geophys. Res.*, 121, 11,113-11,128,
606 doi : 10.1002/2016JA023270

607 Rottman, G.J., N.W. Thomas; W. McClintock, *SORCE solar UV irradiance results*, *Adv. Space Sci.*, 37, 201-208,
608 (2006)

609 [Shaposhnikov, D.S., A.S. Medvedev, A.V. Rodin, and P. Hartogh, Seasonal water “pump” in the atmosphere of](#)
610 [Mars: Vertical transport to the thermosphere, *Geophys. Res. Lett.*, 46, 4161-4169, \(2019\)](#)

611 [Shizgal, B., and R. Blackmore, A collisional kinetic theory of a plane parallel evaporating planetary atmosphere,](#)
612 [*Planet. Space Sci.*, 34, 279-291, \(1986\).](#)

613 Terada, K., N. Terada, H. Shinagawa, H. Fujiwara, Y. Kasaba, K. Seki, F. Leblanc, J-Y. Chaufray, and R. Modolo, A
614 full-particle Martian upper thermosphere-exosphere model using the DSMC method, *J. Geophys. Res.*, 121,
615 1429-1444, doi: 10.1002/2015JE004961, [2016](#)

616 [Vandaele, A.C, O. Korablev, F. Daerden, et al., Martian dust storm impact on atmospheric H₂O and D/H observed by](#)
617 [ExoMars Trace Gas Orbiter, *Nature*, 568, 52, \(2019\)](#)

618 Vidal-Madjar, A., and J-L. Bertaux, A calculated hydrogen distribution in the exosphere, *Planet Space Sci.*, 20, 1147-
619 1162, 1972

620 Yamauchi, M., T. Hara, R. Lundin, E. Dubinin, A. Fedorov, J-A. Sauvaud, R.A. Frahm, R. Ramstad, Y. Futaana, M.
621 Holmstrom, S. Barabash (2015), Seasonal variation of martian pick-up ions: Evidence of breathing exosphere,
622 *Planet. & Sp. Sci.*, 119, p. 54

1 **Study of the hydrogen escape rate at Mars during Martian years 28 and 29 from comparisons between**
2 **SPICAM/Mars Express observations and GCM-LMD simulations**

3 Chaufray, J-Y¹, F. Gonzalez-Galindo², M.A. Lopez-Valverde², F. Forget³, E. Quémerais¹, J-L. Bertaux¹, F.
4 Montmessin¹, M. Chaffin⁴, N. Schneider⁴, J.T. Clarke⁵, F. Leblanc¹, R. Modolo¹, R.V. Yelle⁶

5 ¹*LATMOS, CNRS, Guyancourt, France*, ²*IAA, CSIC, Granada, Spain*, ³*LMD, CNRS, Paris, France*, ⁴*LASP,*
6 *Boulder, CO, USA*, ⁵*Boston University, Boston, MA, USA*, ⁶*University of Arizona, Tucson, AZ, USA*

7
8 Abstract

9
10 We have simulated the 3D atomic hydrogen density in the Martian upper atmosphere and associated Jeans escape rate
11 during Martian years 28 and 29. The coronal Lyman- α brightness is computed using a 3D radiative transfer model
12 which accounts for the monthly average hydrogen density for these two years and is compared to a large set of
13 observations by Mars Express/SPICAM. The simulated brightness is generally in good agreement with the
14 observations for $L_s < 230^\circ$ and $L_s > 330^\circ$ for Martian year 28 and $L_s < 270^\circ$, $L_s > 340^\circ$ for Martian year 29, but the
15 model strongly underestimated the brightness for $230 < L_s < 330^\circ$ for Martian year 28 and $270 < L_s < 340^\circ$ for
16 Martian year 29. In these simulations the transport of water vapor contributes to the production of hydrogen at high
17 altitudes during southern summer. A possible explanation for the model discrepancy is an underestimate of this water
18 transport, associated with an underestimate of the hygropause altitude and/or an underestimate of the supersaturation
19 of the mesosphere. Considering this discrepancy, we estimate the hydrogen escape rate during these two Martian
20 years to vary by almost two orders of magnitude, between $\sim 10^{25}$ to $6 \times 10^{26} \text{ s}^{-1}$ (equivalent to a global layer of water
21 ~ 33 to 2000 mm deep every billion years), in agreement with the seasonal variations estimated directly from the fit
22 of the SPICAM observations during the Martian year 28 by Chaffin et al. (2014). Our analysis suggests that
23 episodic dust storms and associated enhancements at high altitude near perihelion are a major factor in the H escape
24 estimates averaged over one martian year or longer periods, but the accumulated water lost at this rate for 4 billions
25 years is much lower than the amount of water needed to form the flow channels observed on Mars.

26 1) Introduction

27
28 Several geologic and mineralogic observations indicate that Mars was not always as dry as it is today (e.g. Bibring et
29 al. 2006, Bishop et al. 2008, Hynek et al. 2010). The fate of the water is still unknown, but substantial amounts could
30 have escaped into the interplanetary medium in the form of atomic hydrogen (Jakosky et al. 2018). So, understanding

31 of how water currently escapes from Mars is necessary to investigate the long-term evolution of the Martian climate.
32 Recent observations suggest that the amount of exospheric hydrogen at Mars has important seasonal variations, with
33 a larger abundance during southern summer (Chaffin et al. 2014, Clarke et al. 2014, 2017, Bhattacharyya et al. 2015).
34 This increase of the hydrogen density should be associated with an increase of the hydrogen Jeans escape. These
35 seasonal variations have a large impact on the plasma environment of Mars (Bertucci et al. 2013, Yamauchi et al.
36 2015, Romanelli et al. 2015, Halekas 2017, Rahmati et al. 2018), and could be driven by large amounts of water
37 vapor in the mesosphere, as observed by Mars Express/SPICAM (Maltagliati et al. 2017, Fedorova et al. 2018),
38 during dust storm season (Chaffin et al. 2017, Heavens et al. 2018). Using the Global Circulation Model of
39 Laboratoire de Météorologie Dynamique (GCM-LMD) (Forget et al. 1999, Gonzalez-Galindo et al. 2009, 2015), we
40 were able to simulate seasonal variations of the hydrogen escape, but with a lower range than derived from
41 observations (Chaufray et al. 2015a). In order to better characterize the hydrogen exosphere of Mars and the
42 variability of hydrogen escape, we performed a detailed study of the Martian years 28 and 29, and compared the
43 simulated brightness to a large SPICAM Lyman- α dataset during the same two years. The year number used in this
44 study follows the convention chosen by Clancy et al. (2000) with April 11 1955 ($L_s=0^\circ$) chosen as the beginning of
45 the Martian year 1.

46 The data used in this study is described in section 2. In section 3, we present our 3D simulated Lyman- α emissions
47 corresponding to the Martian years 28 and 29, which are obtained by coupling several models. The comparisons
48 between the observed and simulated Lyman- α profiles are presented in section 4 and the possible origin of the
49 discrepancy is discussed in section 5, followed by conclusions in the last section.

50 2) Observations

51
52 The Spectroscopy for Investigation and Characterization of the Atmosphere of Mars (SPICAM) is a dual ultraviolet
53 and infrared spectrometer aboard Mars Express (Bertaux et al. 2006, Montmessin et al. 2017). The ultraviolet channel
54 uses an optical entrance of 4 cm diameter feeding an off-axis parabolic mirror which focuses the observed scene at
55 the focal plane. The instantaneous field of view (IFOV) is limited at the focal point of the parabolic mirror by a 50
56 μm wide retractable slit that extends over an angular aperture of 2.8° , equivalent to about two pixels on the UV
57 detector. In the upper most portion of the slit, a 10 times wider aperture allows for the observations of fainter sources
58 at the expense of degraded spectral resolution.

59 In principle, SPICAM can record 288 spatially resolved spectra along the slit. However, to save data volume
60 transmission, only 5 spectra are transmitted each second. For all the observations presented here, the spectra are the
61 sum of 32 individual CCD line spectra forming 5 adjacent spatial bins of 0.32° each, starting from the CCD line Y_0 .
62 The wavelength range of the UV channel is 118 – 320 nm and includes the strong hydrogen Lyman- α emission line at
63 121.6 nm. This emission line is produced by resonant scattering of solar photons by hydrogen atoms in the Martian
64 upper atmosphere. Such emission is observed over several Martian radii as a signature of the extended hydrogen
65 exosphere of Mars (Chaufray et al. 2008).

66 We selected several observations obtained during the Martian years 28 (from 22 Jan 2006 to 9 Dec 2007) and 29
67 (from 10 Dec 2007 to 26 Oct 2009) performed by the UV spectrograph SPICAM on Mars Express, including those
68 studied by Chaffin et al. (2014). During this period the UV channel exhibited an anomalous image intensifier
69 behavior, leading to sporadic changes of the high voltage during a sequence of observations (Montmessin et al.
70 2017). We selected by visual inspection the observations least affected by this behavior. A cleaning procedure has
71 been developed to flag the UV channel spectra affected by these high voltage spikes (Montmessin et al. 2017). All
72 these flagged spectra have been removed from use in this study.

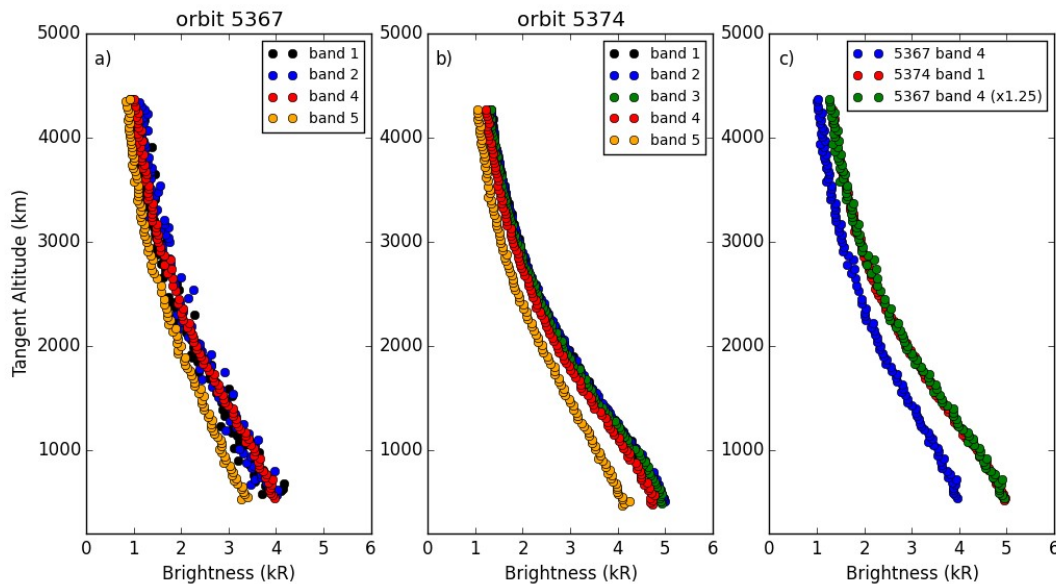
73 The list of observations used for this study is summarized in Tables 1 and 2 in the Appendix.

74 Some of the observations were performed without the slit, while others were performed with the slit. Also, the 5 CCD
75 spatial bands (corresponding to a binning of 32 individual, consecutive lines) transmitted each second can differ
76 between observations. Three different configurations are used in the observations presented here. The first
77 configuration corresponds to an observation with the slit and starts from CCD line $Y_0 = 23$, the second configuration
78 also corresponds to an observation with the slit, but starts from CCD line $Y_0 = 118$, and the third configuration
79 corresponds to an observation without the slit, starting from CCD line $Y_0 = 118$.

80 For the first configuration, all the transmitted bands correspond to the part of the CCD in front of the narrow part of
81 the slit, so we chose band 5, which is close to the center of the CCD (lines 118- 149). For the second configuration,
82 the last two bands correspond to the part of the CCD in front of the large part of the slit. The signal to noise ratio is
83 generally better, and straylight near 132 and 143 nm discussed by Leblanc et al. (2006) and Chaufray et al. (2009) is
84 not detected in those bands. Therefore, we chose band 4 (lines 214-245), which is more sensitive than band 5 by
85 about 20% (Fig. 1a). For the last configuration without the slit, we chose band 1, which corresponds to the same CCD
86 lines as configuration 1 (lines 118-149), but is slightly different (by about 5%) than the derived brightness from band

87 4 (lines 214-245) (Fig. 1b). As shown in Fig. 1, the signal to noise ratio of the derived brightness profile is very good
 88 and trying to improve it by using the 5 transmitted bands will not change our results since the calibration uncertainty
 89 is larger than the standard deviation of the measurement.

90

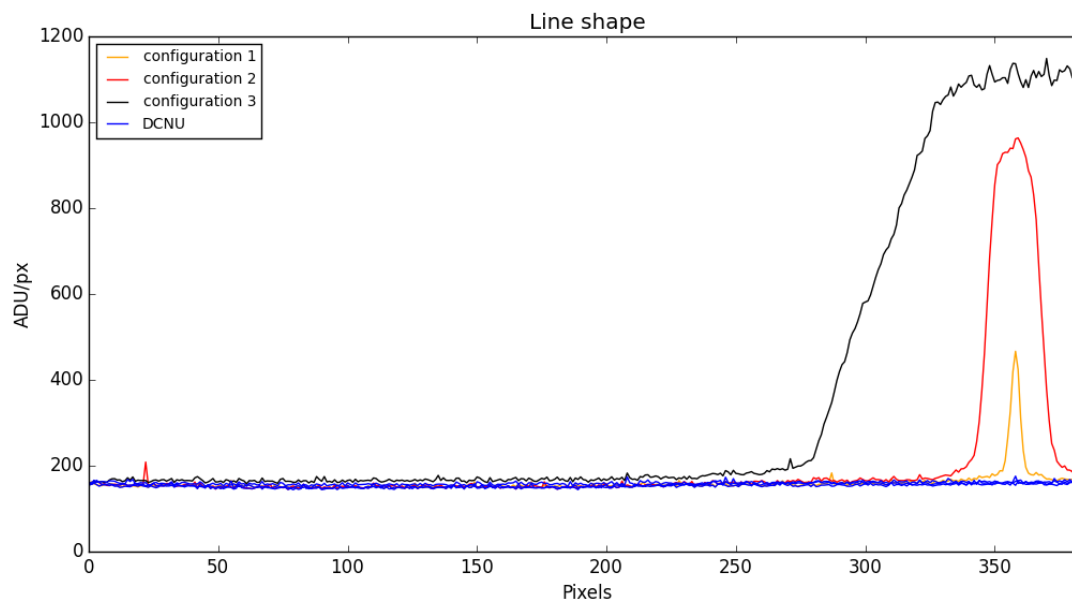


91 *Fig. 1 : a) Brightness profiles derived from Mars Express orbit 5367 with the slit over the first 2 and last 2*
 92 *transmitted bands of the CCD. b) Brightness profiles derived from Mars Express orbit 5374 without the slit over the*
 93 *5 transmitted bands. c) Comparison between the profiles derived from the two orbits over the bands used in this*
 94 *study considering a 1.25 factor for the observations with the slit*

95 Observations with very similar geometries (orbits 5367 and 5374 for example, Fig. 1) obtained with and without the
 96 slit, indicate a systematic $\sim 20\%$ underestimate of the derived brightness with the slit compared to the observations
 97 without the slit (Fig. 1b). 5% could be attributed to the different CCD lines as suggested by Fig. 1b. The rest of the
 98 difference could come from the method used to integrate the spectral line, neglecting the extended spectral wings, or
 99 in a continuum background subtraction. Therefore, to summarize, the brightness measured by configuration 3 is used
 100 as a reference, and a correction by 20% is applied to the brightness measured in configuration 1 and a correction of
 101 25% is applied to the brightness measured by configuration 2. Examples of Lyman- α vertical profiles are displayed in
 102 Fig. 1.

103 The spectral shape of the Lyman- α line measured for each configuration is displayed in Fig. 2. For the first two
 104 configurations, the brightness is computed by integration over the line profile after subtraction of a residual linear
 105 background (Chaufray et al. 2008). For the third (slitless) configuration, the average number of counts per pixel is
 106 computed and converted to Rayleighs using the solid angle defined by one pixel. All spectra have been corrected for

107 the offset and Dark Charge non-uniformity (DCNU) (see Bertaux et al. 2006 for more details).



108

109 *Fig. 2 Spectral shape of the Lyman- α line measured for the three configuration used in the paper. These spectral*
110 *profile correspond to the average observation between 2000 and 2200 km from observation 5367 (narrow slit :*
111 *configuration 1 and large slit : configuration 2) and observation 5374 (no slit : configuration 3). A sapphire filter is*
112 *glued above the CCD MgF₂ input window, preventing Lyman- α photons to reach pixels < 250 without slit (Bertaux et*
113 *al. 2006). With the slit, the linewidth is constrained by the slit size. The Dark charge non-uniformity (DCNU) is also*
114 *indicated in blue and is very similar for these three measured spectra.*

115 Such a systematic uncertainty is in the range of the absolute calibration of the instrument from star observations
116 (Montmessin et al. 2017). Therefore, in this study we focus on systematic differences between the observations and
117 the simulations which are >25%, as well as the differences in the shape of the observed and simulated vertical
118 variations.

119 **3) Models**

120

121 To simulate the hydrogen corona of Mars during Martian years 28 and 29, we used three models. The first model is
122 the GCM-LMD describing the Martian atmosphere from the surface to the exobase (Forget et al. 1999, Gonzalez-
123 Galindo et al. 2009, 2015), including the hydrogen in the thermosphere (Chaufray et al. 2015a, 2018). The second
124 model is an exospheric model considering nonuniform conditions at the exobase (hydrogen density and temperature
125 from the GCM-LMD) to derive the hydrogen density in the exosphere, based on the approach of Vidal-Madjar and
126 Bertaux 1972. The last model is a 3D Monte Carlo radiative transfer model used to simulate the resonance Lyman- α

127 spectral volume emission rate (Chaufray et al 2015b). The Lyman- α brightness is computed by formal integration of
128 the radiative transfer equation using simulated volume emission rates for the specific geometry (spacecraft position
129 and line of sight direction) of each individual observation listed in Tables 1 and 2 in Appendix A. The simulated
130 brightness is directly proportional to the solar flux at the center of the solar Lyman- α line. To derive it, we used the
131 solar brightness between 121-122 nm measured by SORCE (Rottman et al. 2006) rescaled to Mars distance, with
132 accounting for the different ecliptic longitudes of Earth and Mars as seen from the Sun. The brightness at the center
133 of the line is derived from the empirical relation given by Emerich et al. (2005). The variability of the solar flux
134 between 121 and 122 nm measured by SORCE during the full period is $\sim 10\%$, therefore uncertainty on the flux at
135 Mars, due to the different ecliptic longitudes of Mars and Earth should be at most $\sim 10\%$ but could differ from one
136 observation to the other. Due to the large CPU time required by the Monte Carlo radiative transfer simulations, it is
137 not possible to simulate the Martian Lyman- α volume emission rate with every GCM-LMD time step. In this study,
138 we consider only monthly average hydrogen for the exosphere and corona. This is another source of uncertainty in
139 the simulated brightness that prevents us from discussing differences less than a few tenths percent in the brightness
140 comparisons. This resolution is enough to discuss the seasonal variations that are important, as observed from several
141 missions (Chaffin et al. 2014, 2018, Clarke et al. 2014, Battacharyya et al. 2015, 2017).

142 **3.1) Thermospheric density**

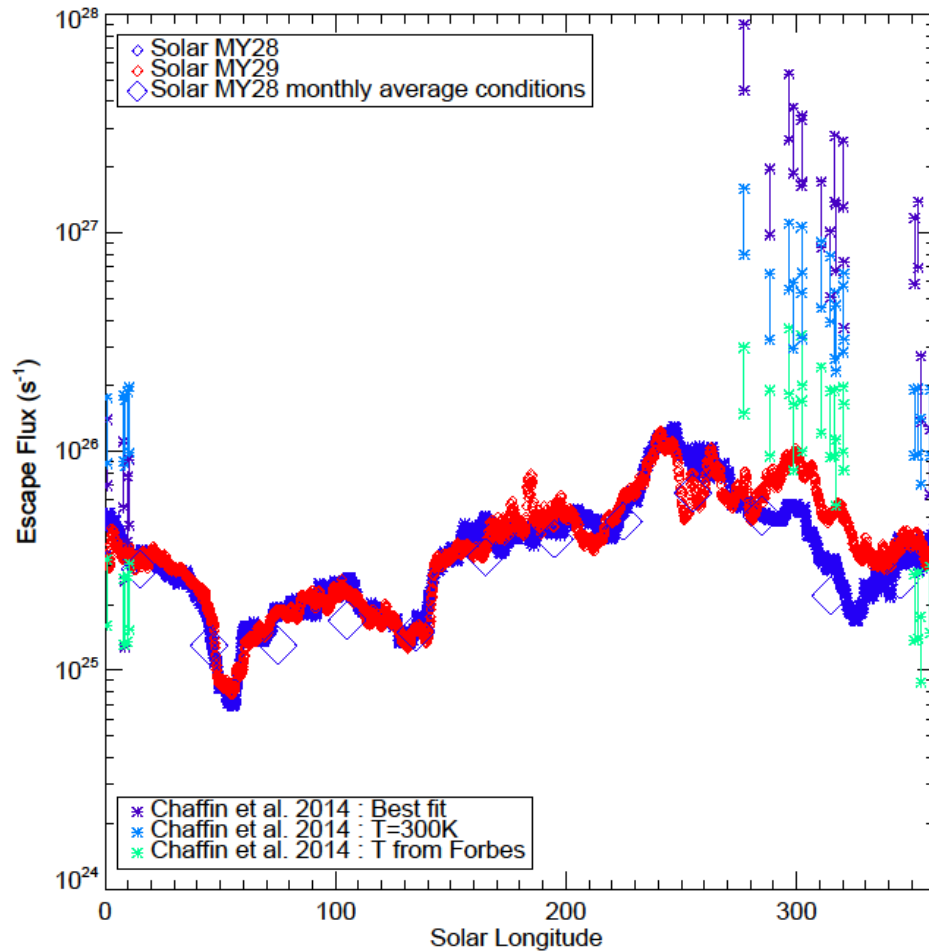
143
144 The GCM-LMD is a 3D model of the Martian atmosphere from the surface to the exobase. It is composed of a 3D
145 dynamics core which solves the fluid equations over a sphere and a physical core, describing all the physical
146 processes computed for each column. In all the simulations presented below, the horizontal resolution is 5.625° in
147 longitude and 3.75° in latitude. The dynamical time step δt is 1 sol/960. ~ 1.5 minute, and the physics time step is Δt
148 $= 5\delta t \sim 7.5$ minutes. More details on the GCM-LMD can be found in Forget et al. (1999) and Gonzalez-Galindo et al.
149 (2009, 2015). As noted in Chaufray et al. (2015a) the vertical resolution used in the molecular diffusion (2 km) can
150 lead to an uncertainty of a few tenths in the hydrogen density above 200 km, depending on the season and martian
151 year. Because we will focus on large differences between the simulated brightness and observed brightness, this
152 uncertainty as a monthly average exosphere, should not change our conclusion.

153 In these simulations, we account for the daily variations of the solar flux during the Martian year 28 and 29 as
154 computed by Gonzalez-Galindo et al. (2015). We also consider the dust scenarios of these years derived by

155 Montabone et al. (2015). We do not include the microphysical processes controlling the supersaturation presented in
156 Navarro et al. (2014), as these results, and especially the hydrogen density in the Martian thermosphere, depend on
157 model parameters not well constrained by the observations. These simulations will be discussed in section 5. We also
158 do not include the coupling with the exospheric ballistic transport developed by Chaufray et al. (2018). This coupling
159 can't be performed for a full Martian year because of the large CPU time needed. The first few studies we performed
160 indicate that the effect on the brightness should not be greater than a few tens of percent, and therefore, the
161 differences discussed in section 5 should still be present with this coupling. A study of the local time variations
162 would require such a coupling. Therefore, in this paper we will focus on the seasonal variation of the hydrogen
163 corona and escape. We only consider the hydrogen Jeans escape, computed assuming a
164 Maxwellian distribution at the upper level. Shizgal and Blackmore (1986) have shown that
165 the depletion of energetic atoms could reduce the real escape rate by a factor ~ 0.57 for an
166 exospheric temperature of 230 K and 0.53 for an exospheric temperature of 310 K, We also
167 neglect the non-thermal escape processes which should be not very efficient for atomic
168 hydrogen compared to the thermal escape rate (Krasnopolsky 2010). The non-thermal escape
169 of molecular hydrogen was discussed in Krasnopolsky (2017) and Chaufray et al. (2017)
170 and is not included in these simulations.

171 The simulated escape flux for the Martian years 28 and 29, as well as the escape flux derived from the monthly
172 average conditions for Martian year 28 are displayed on Fig.2. These variations are close to the simulated escape
173 rates for solar minimum conditions by Chaufray et al. (2015a; 2018) as expected for these Martian years.

174



175
 176 *Fig. 3 : Jeans hydrogen escape rate simulated for the Martian years 28 (blue) and 29 (red) with the GCM-LMD. The*
 177 *escape rate derived from the monthly average upper atmosphere are also indicated by the blue diamonds. The escape*
 178 *rates derived from SPICAM fit (from observations between end of Martian year 28, beginning of Martian year 29)*
 179 *using different assumptions by Chaffin et al. 2014 are also displayed. The escape flux (at/cm²/s) was converted to*
 180 *escape rate (at/s). For this conversion, we assume either a uniform flux at the exobase or a uniform flux at the*
 181 *dayside exobase and no escape flux at the nightside, leading to the range given by each vertical line.*

182 **3.2) Exospheric density**

183
 184 The hydrogen density is extended to the exosphere (above 200 km), by solving the Liouville equations from non-
 185 uniform conditions at the exobase (Vidal-Madjar and Bertaux 1972). We consider Maxwellian velocity
 186 distribution functions at the exobase using the temperature and the hydrogen density computed from the LMD-GCM
 187 reinterpolated at 200 km as done in our previous simulations (Chaufray et al. 2015a, 2018). The real distribution at
 188 the exobase should differ from a Maxwellian distribution. Due to the escaping particles, the Maxwellian distribution
 189 is truncated at velocity larger than the escape velocity (Shizgal and Blackmore 1986, Boqueho et al. 2005, Terada et
 190 al., 2016). However, this truncation should not affect the ballistic distribution with a velocity lower than the escaping

191 velocity but only reduce the escape rate (Brinkmann, 1970). The Direct Simulation Monte Carlo method used by
192 Terada et al. (2016) shows that the ballistic hydrogen population is very close to the Maxwellian distribution at the
193 local temperature (see Fig 8b in Terada et al. 2016).

194 In the computation of the exospheric hydrogen density we neglect ionization loss and the effect of solar radiation
195 pressure that should be important at a few Martian radii above the altitudes scanned by the missions and the optically
196 thick region of the hydrogen corona (Beth et al. 2014).

197 **3.3) Radiative transfer model for resonance line**

198
199 The computation of the Lyman- α brightness is done in two steps, as done by numerous models (e.g., Gladstone
200 1992). In a first step, we use a 3D Monte Carlo radiative transfer model to compute the 3D volume emission rate
201 from 80 km to 50,000 km. This radiative transfer model is a 3D version of the model used by Chaufray et al. (2012,
202 2015b) to study the hydrogen corona of Venus, which accounts for angle-dependent partial frequency redistribution
203 (Lee 1982) and describes the spectral line from -5 to +5 Doppler width (at the maximum temperature at the exobase,
204 i.e., $\sim \pm 40$ m/s).

205 The brightness is then computed in a second step, rescaling the volume emission rate to the solar flux at Lyman- α at
206 the time of the observations and accounting for the geometry of each individual observation from Mars Express
207 (Chaufray et al. 2008). Twenty-four 3D volume emission rates, monthly average, corresponding to Martian months of
208 the years 28 and 29 have been computed. To reduce the CPU time, we did not simulate every line of sight for
209 each observation, but instead averaged several lines of sight (between 5 and 20) and compared the simulated
210 brightness of the average line of sight with the observed average brightness.

211 The interplanetary brightness emission is estimated for each individual observation using a 3D radiative transfer
212 model of the interplanetary emission (Qu  merais 2000). The possible uncertainty on the brightness should be small
213 ($\sim 100\%$) compared to the brightness of the Martian hydrogen corona and will not change the conclusion of this
214 study.

215 **3.4) Effect of ballistic transport in the Martian exosphere**

216
217 The effect of ballistic transport on the hydrogen density near the exobase of Mars has been recently studied
218 (Chaufray et al. 2018). This coupling has not been included in this study due to the large CPU needed to perform
219 such coupled simulations. Our first estimates indicate that considering this coupling has a small effect on the

220 simulated brightness. The Lyman- α emission line is optically thick below few thousands kilometers in altitude
 221 (Bhattacharyya et al. 2017) and therefore is sensitive to global conditions and not too significantly affected by local
 222 conditions. Ballistic transport redistributes the hydrogen atoms in the exosphere, but does not change the global
 223 amount of hydrogen in the exosphere. Therefore, it is not surprising to find a limited impact on the simulated
 224 brightness. Since the main goal of this study is to focus on the large differences between the simulations and the
 225 observations, in the next section we will neglect this effect. A more careful study of the local time variations by few
 226 tenths of the brightness as observed by MAVEN (Chaffin et al. 2015) would need to include this effect and such a
 227 study is therefore deferred to a future work.

228

229 **4) Comparisons with observations**

230 Examples of comparisons between the observed brightness and the simulated brightness at different Martian months
 231 are displayed on Fig. 4. The model reasonably reproduces the observations at $L_s = 180^\circ$, 220° and 340° but
 232 underestimates the brightness at $L_s = 280^\circ$ and does not reproduce the shape of the vertical profile. To quantify the
 233 difference between the observed and simulated brightness, we derived an optimized scale factor which needed to be
 234 applied to the observation to better reproduce the simulated profile by minimizing the function.

$$235 \quad \Delta^2 = \sum_{los} [\log(I_{obs}) + \log(A) - \log(I_{sim})]^2$$

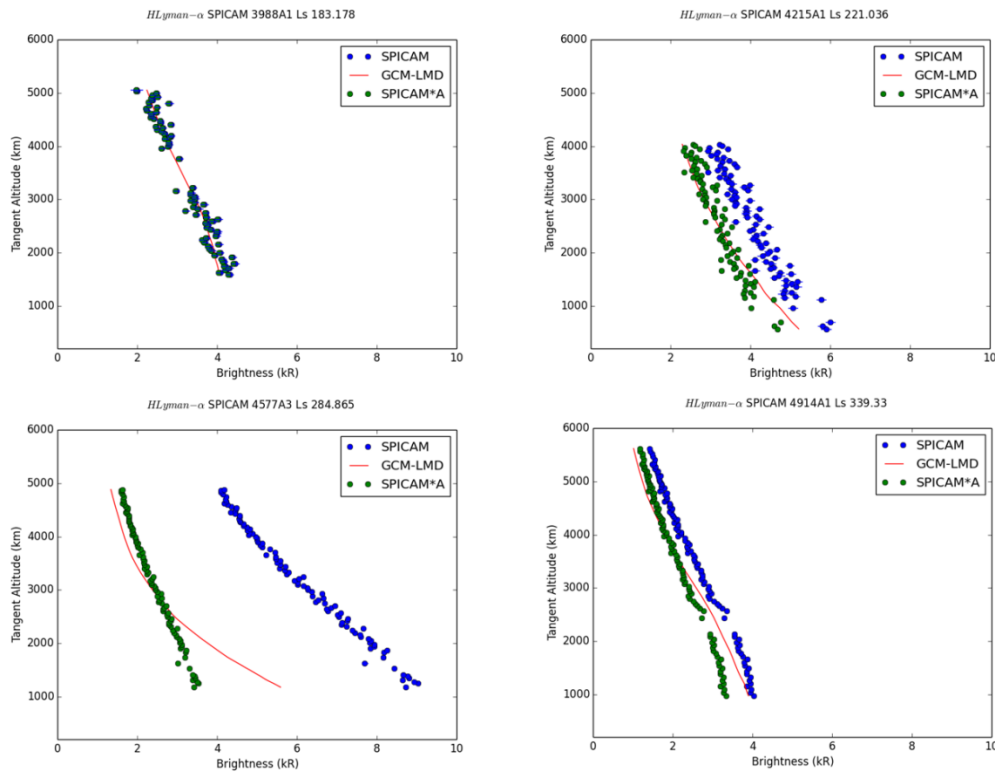
236 The minimum of the function Δ^2 is found when its derivative $\partial\Delta^2/\partial A = 0$ yielding A as

$$237 \quad \log(A) = \frac{1}{n} \sum_{los} [\log(I_{sim}) - \log(I_{obs})]$$

238 The rescaled profile is also displayed on Fig.4. For the three observations at $L_s = 180^\circ$, 220° and 340° displayed in
 239 Fig. 4, this scale factor is 0.99, 0.79, and 0.82 respectively, and is in the range of possible uncertainty associated with
 240 the retrieved brightness and the solar flux at Mars or the simulation of a monthly average hydrogen corona. For the
 241 observation near $L_s = 280^\circ$, the scale factor is 0.39, which cannot be explained by the uncertainty in the retrieved
 242 brightness by SPICAM-UV.

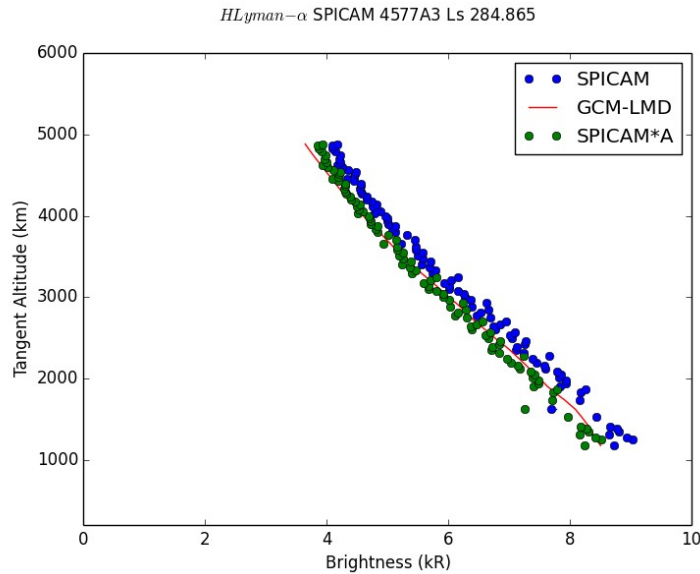
243 The difference between the simulated and the observed Lyman- α brightness indicates an important underestimate of
 244 the hydrogen density by the model, as was suggested by our first simple comparison of the escape rate derived from
 245 SPICAM by Chaffin et al. (2014) at this season (from the same set of observations) and the simulated escape rate for
 246 different solar conditions (Chaufray et al. 2015a). The shape of the simulated profile also differs from that of the

247 observed profile, confirming that the difference cannot be attributed to the absolute calibration of SPICAM or an
 248 underestimate of the solar flux at Mars and is therefore due to an underestimate of the hydrogen density at this season
 249 by our model. Observations performed simultaneously between $L_s = 331$ and 345° by HST during the Martian year
 250 28 also indicate a decrease of the hydrogen corona from this period (Clarke et al. 2014), which is consistent with the
 251 SPICAM observations.
 252 Possible explanations of this underestimate of the hydrogen content of the Martian upper atmosphere in our model
 253 will be discussed in section 5



254
 255 *Fig. 4 Examples of comparisons between the Lyman- α brightness profiles observed by SPICAM-UV (blue dots) and*
 256 *the simulated brightness profile (red line) for different solar longitude L_s during the Martian year 28.*

257 Fig. 5 displays the simulated profile corresponding to observation 4577 when the simulated hydrogen density is
 258 arbitrarily multiplied by a factor 6. In that case, the simulated profile is in better agreement with the observation and
 259 the simulated shape of the profile is consistent with the observed shape, confirming the difference is likely due to an
 260 underestimate of the hydrogen density by the model.

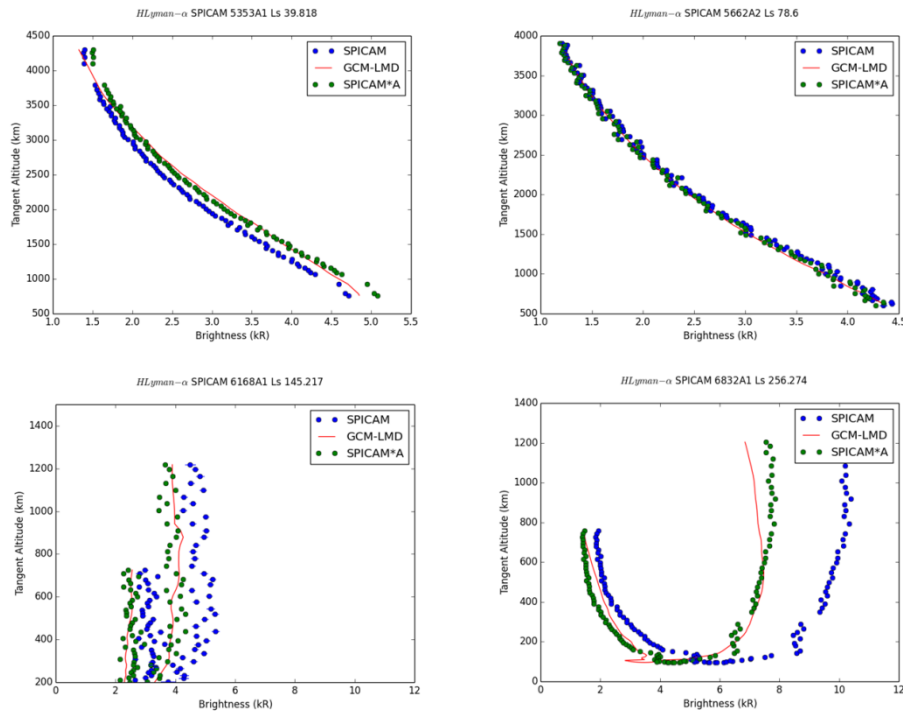


262 *Fig. 5 Simulated Lyman- α brightness profile for orbit #4577 with a simulated hydrogen density multiplied by 6*
 263 *w.r.t. the normal model, compared to the SPICAM*

264 Examples of comparisons between the observed brightness and the simulated brightness at different Martian months
 265 for Martian year 29 are displayed on Fig. 6. The model reasonably reproduces the observations at Ls near 40° , 80°
 266 (the best comparison for the full set of observations), and to a lesser extent, near 145° , but fails to reproduce
 267 the observation near Ls= 255° . The observation at Ls= 255° corresponds to a grazing limb observation with a tangent
 268 altitude decreasing at the nightside (brightness $< 4\text{kR}$) reaching a minimum altitude near 100 km and increasing on
 269 the dayside where the Lyman-alpha brightness is large, $\sim 10\text{kR}$.

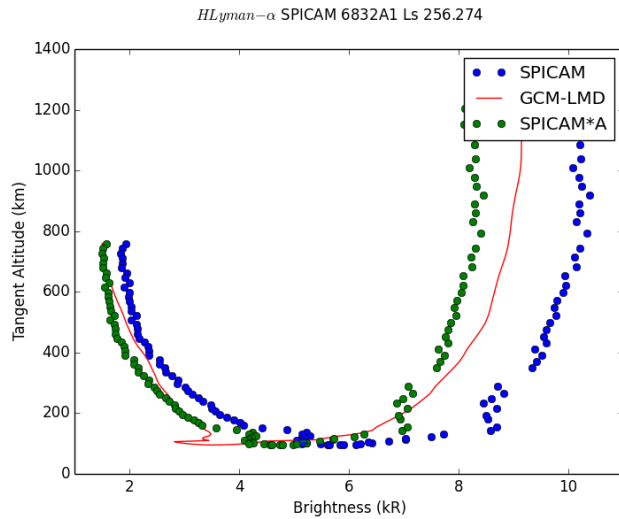
270 For the Martian year 29, we derive an optimized scale factor A for each observation. The scale factors are 1.08, 0.98,
 271 0.81 and 0.75 for the four profiles displayed on Fig. 5., confirming that the model underestimates the brightness near
 272 summer southern solstice. While the factor 0.75 is close to the reasonable value, it corresponds to a large difference
 273 in term of hydrogen density, due to the large brightness ($\sim 10\text{kR}$) and the non-linearity between the density and the
 274 brightness for an optically thick emission.

275 As for the Martian year 28, we performed another simulation with the hydrogen density arbitrarily multiplied by 6
 276 for the observation #6832. Fig. 7 shows that the agreement is slightly better, as expected, but the brightness is still
 277 underestimated. But the remaining difference is less than 1kR and could be due to the deuterium emission not
 278 included in our simulations, this could possibly be important at this season at these low altitudes (Clarke et al. 2017,
 279 Chaffin et al. 2018).



280

281 *Fig. 6 Examples of comparisons between the Lyman- α brightness profiles observed by SPICAM- UV (blue dots) and*
 282 *the simulated brightness profile (red line) for different solar longitude Ls during the Martian year 29*



283

284 *Fig. 7 Simulated Lyman- α brightness profile for orbit #6832 with a simulated hydrogen density multiplied by 6 w.r.t.*
 285 *the normal model, compared to the SPICAM*

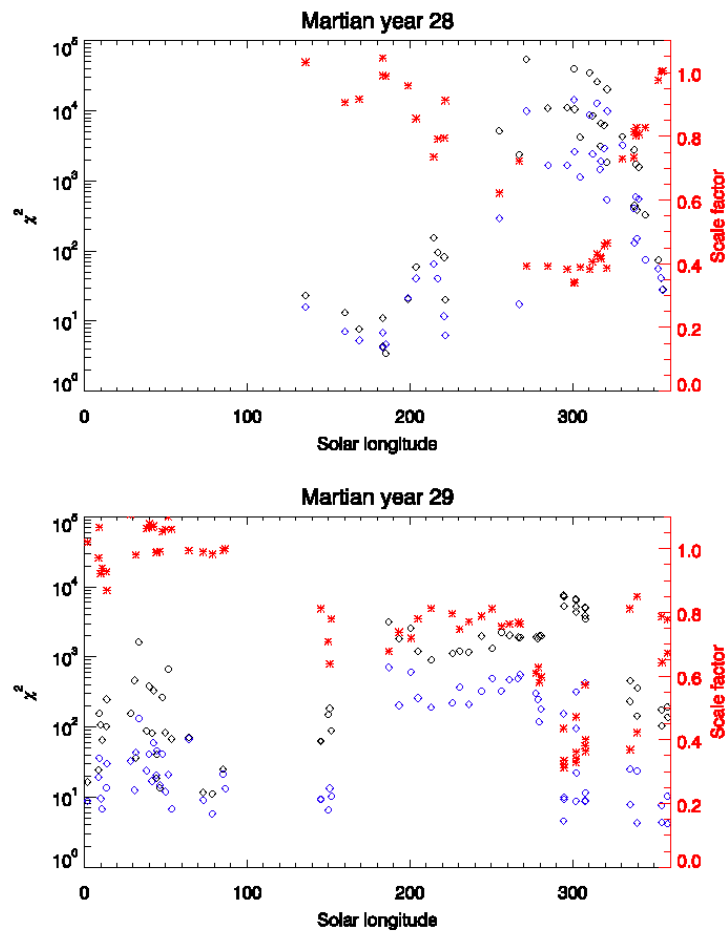
286 For each observation from Martian years 28 and 29, we derive a scale factor and compute the χ^2
 287 value for the observed and the rescaled profiles given by :

$$288 \quad \chi^2 = \frac{1}{n} \sum_{los} \frac{[B * I_{obs} - I_{sim}]^2}{B^2 \sigma_{obs}^2}$$

289 with $B = 1$ for the observed profile and $B = A$ for the rescaled profile.

290 Fig.8 displayed the χ^2 value versus Ls, including all observations given in Table 1, as well as the scale factor A

291 derived from each observation



292

293 *Fig. 8 χ^2 variations (black diamond, left scale) for the Martian year 28 (top) and Martian year (29), and best scale*
294 *factor variations (red crosses, right scale), with the associated χ^2 values (blue diamonds).*

295

296 The full set of observations confirm the conclusion derived from the few examples shown in Figs. 4 and 6. The
297 simulated profiles are in reasonable agreement with the observed profile when $\chi^2 < 100$, and the scale factor is larger
298 than 0.8 ($L_s < 230^\circ$ and $L_s > 330^\circ$) for Martian year 28, and $L_s < 150^\circ$ and $L_s > 340^\circ$ for Martian year 29). The scale
299 factor reaches the smallest values $\sim 0.3-0.4$ for $L_s = 250^\circ - 330^\circ$ for both years, meaning the model strongly
300 underestimates the hydrogen density for this season. For Martian year 28, even if the absolute brightness was
301 rescaled, the shape of the profile would not be well reproduced as indicated by the large value of χ^2 (see also Fig. 4
302 bottom left) when the optimized scale factor is included. To reproduce the observed profile, the simulated hydrogen
303 density should be multiplied by ~ 6 as shown for orbit 4577 in Fig. 5.

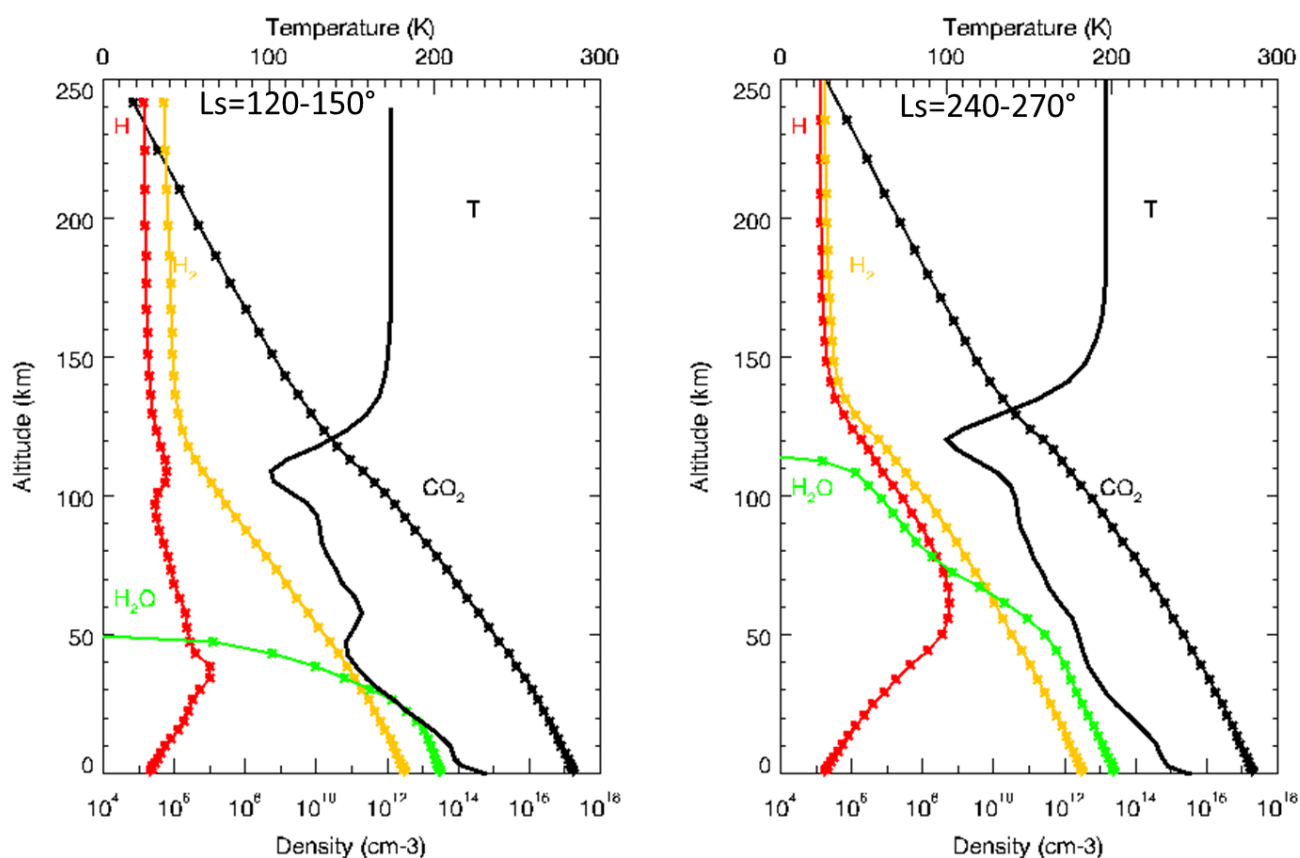
304 At L_s near 0° (observation #5070), Chaffin et al. (2014) was able to fit the observed profile with an escape flux
305 between 1×10^7 and $1 \times 10^8 \text{ cm}^{-2}\text{s}^{-1}$, corresponding to a total escape rate $\sim 1.6 \times 10^{25}$ and $1.6 \times 10^{26} \text{ s}^{-1}$ if we assume a

306 uniform escape flux at the exobase in agreement with our simulated escape rate equal to $4 \times 10^{25} \text{ s}^{-1}$ at this season (Fig.
307 3). The escape flux simulated is not uniform and larger at the dayside than nightside (Chaufray et al. 2015a). If we
308 integrate only the escape flux at the dayside to derive the escape rate, then all the derived escape rate from SPICAM
309 shown in Fig. 3 should be divided by two. In that case, the observations near $L_s=0^\circ$ are still in agreement with our
310 simulations. The two other observations detailed in Chaffin et al. (2014) (observation #4646 and #4501) are not
311 reproduced by our simulations and the escape rate derived by Chaffin et al. (2014) was between 2×10^8 and $5 \times 10^9 \text{ cm}^{-2}$
312 s^{-1} (3×10^{26} and $8 \times 10^{27} \text{ s}^{-1}$) for observation #4501 ($L_s = 271^\circ$) and between 1×10^8 and $2 \times 10^9 \text{ cm}^{-2} \text{ s}^{-1}$ ($1.6 \times 10^{26} \text{ s}^{-1} -$
313 $3.2 \times 10^{27} \text{ s}^{-1}$) for observation #4646 ($L_s = 296^\circ$), larger than our simulated escape flux of $\sim 10^{26} \text{ s}^{-1}$ at these periods
314 (Fig. 2). These high values would be in better agreement with the model escape flux if the simulated hydrogen
315 density was increased by a factor ~ 6 as suggested by our simple density rescale.

316 **5) Discussion**

317 The hydrogen density in the Martian upper atmosphere simulated for Martian years 28 and 29 is in general in
318 reasonable agreement with the SPICAM observations suggesting that the main source processes of atomic hydrogen
319 are included in these simulations during most of the Martian year, except near southern summer solstice ($L_s \sim 270^\circ$).
320 At this period, the hydrogen density and the escape rate are likely underestimated by a factor ~ 6 .
321 At this period, deuterium Lyman- α could contribute partly to the brightness, especially in the thermosphere / lower
322 exosphere as shown by MAVEN/IUVS (Clarke et al. 2017), for example for orbits 6500s, 6600s and 6700s (Fig. 6
323 bottom right). However, the deuterium brightness measured by MAVEN/IUVS during Martian year 32 is less than 1
324 kRayleigh and decreases quickly with altitude, becoming negligible above 300 km. Such a low brightness is
325 insufficient to explain the discrepancy between the model and the observations. Substantial amounts of water vapor at
326 high altitude in the mesosphere has been detected by SPICAM at this season (Maltagliati et al. 2013, Fedorova et al.
327 2018). The water vapor could be photodissociated and contribute to an increase in the hydrogen density in the
328 Martian thermosphere and exosphere, as well as the hydrogen escape (Chaffin et al. 2017). The MAVEN/NGIMS
329 ionospheric observation above 150 km near the same season (Martian year 32) suggested a water vapor mixing ratio
330 of only 0.4 ppb at 80 km, in order to avoid the loss of observed HCO^+ by H_2O reactions (Fox et al. 2015), but has
331 been recently questioned by another model (Krasnopolsky 2019). In this study, the water vapor density profile was
332 assumed to be close to a diffusion equilibrium profile. Recently, Heavens et al. (2018) suggested that the increase of
333 the hygropause altitude due to dust storms could lead to an increase of the hydrogen density (and escape) in the

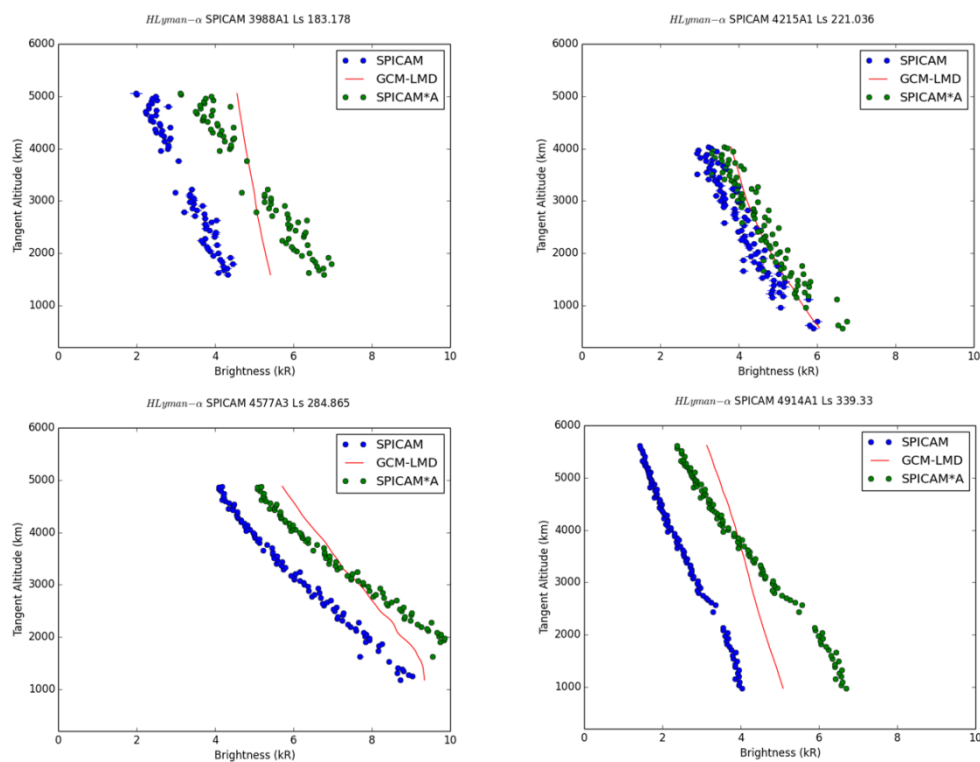
334 thermosphere, while Shaposhnikov et al. (2019) suggest, using a GCM, that a “pump” mechanism could facilitate
 335 upward transport at high latitude during perihelion. Seasonal variations of the hygropause at Mars are
 336 present in the LMD-GCM simulations (Montmessin et al. 2005). Fig. 9 displays a typical density profile for H, H₂,
 337 H₂O, and CO₂ and the temperature profile obtained for Martian year 28 at the equator at noon for the month Ls =
 338 120-150 and Ls = 270° - 300°. At Ls = 120-150°, the water vapor is confined to very low altitudes (< 20 km). The
 339 hydrogen density presents a double-peaked profile, one peak in the low atmosphere due to water vapor
 340 photodissociation, and another peak in the low thermosphere due to ionospheric reactions (Krasnopolsky 2002). At
 341 Ls=240-270°, the hygropause is ~ 50 km, but there are still substantial amounts of water vapor in the mesosphere
 342 near 80 km but not above 120 km. Only one hydrogen density peak is observed, because the peak associated with
 343 ionospheric reactions is merged with the hydrogen coming from water photodissociation transported from the lower
 344 atmosphere which is ~100 times larger.



345
 346 *Fig. 9 Vertical density profile of the main hydrogen species and CO₂ at noon equator from the surface to the exobase*
 347 *simulated for two different months during the Martian year 28.*

348
 349 The dissociation of water vapor is a source of atomic hydrogen in the Martian lower thermosphere. Such an effect

350 could be the main driver of our simulated escape rate, contrary to our first interpretation (Chaufray et al. 2015a). This
 351 would partly explain the difference between our simulations and the model of Krasnopolsky (2002), as suggested by
 352 Krasnopolsky (2017). An increase in the water vapor density could explain the current underestimate of the hydrogen
 353 escape at $L_s = 270^\circ$ - 300° , and would be in agreement with the conclusion of Maltagliati et al. (2013), who found that
 354 the GCM-LMD underestimates the water vapor in the Martian mesosphere at this season, since the description of the
 355 water cycle presented in this study is done with similar assumptions than those used by these authors. This
 356 discrepancy was attributed to an underestimation of the strength of the interaction between the water vapor and the
 357 dust cycles. The water vapor mixing ratio in the mesosphere depends on the supersaturation of the upper atmosphere,
 358 which is not well known. The microphysical processes controlling supersaturation are now included in the LMD-
 359 GCM (Navarro et al. 2014), but their effects on the water vapor at high altitudes depends on model parameters not
 360 well constrained by the observations and therefore were not included in these simulations. A similar comparison with
 361 the few SPICAM observations displayed in Fig. 4 of the simulations used to generate the Mars Climate Database 5.2
 362 (for the Martian year 28), including these microphysical processes is displayed in Fig. 10



363
 364 *Fig. 10 Same as Fig. 4 but for the simulations used to generate the MCD 5.2, including the microphysical processes*
 365 *controlling the supersaturation.*

367 In these simulations, the Lyman-alpha brightness is overestimated, even at the southern summer. The brightness

368 profiles for observations 4215A1 is in good agreement, while the simulated shape profiles of the three other
369 observations is very different from the observed shape suggesting that the difference is due to an overestimate of the
370 hydrogen density in the Martian upper altitude. The average hydrogen escape rate for $L_s = 270\text{-}300^\circ$ used to simulate
371 the observation 4501 is $1.1 \times 10^{27} \text{ s}^{-1}$, larger by ~ 2 compared with the escape rate estimated in section 4 after a global
372 rescale of the hydrogen density. Although not perfect, the updated LMD-GCM microphysical processes could be
373 sufficient to produce the large amount of hydrogen lacking in our previous simulations. Our simulations could also be
374 consistent with the ionospheric observations by MAVEN/NGIMS, because if the amount of water vapor coming from
375 the lower atmosphere is larger at 120 km, but remains negligible above 150 km, it could prevent the HCO^+
376 destruction while producing H_3O^+ ions near 120 km (Fox et al. 2015). A more detailed study of the link between the
377 water vapor and the atomic hydrogen and ionospheric water species will benefit from future observations of the water
378 vapor density in the Martian mesosphere/thermosphere by Exo Mars Trace Gas Orbiter (Lopez-Valverde et al. 2018),
379 especially during the recent global dust storm in June 2018. Comparisons of other Martian years like Martian year 32
380 where an increase of water vapor was also observed by SPICAM (Fedorova et al. 2018), and using the large Lyman- α
381 dataset of MAVEN/IUVS (Chaffin et al. 2015, 2018) will be also useful to estimate the year to year variability
382 possibly due to dust events and the variability associated with the solar activity in order to extrapolate past conditions
383 with larger EUV solar flux and orbit parameters. Space weather events also increase the atmospheric escape rates
384 (Jakosky et al. 2015). But they mostly increase the heavy ions escape rates as reported in Jakosky et al. (2015)
385 during the interplanetary coronal mass ejection in March 2015. Solar flares could heat the Martian upper atmosphere
386 and increase the escape rate during short time periods (Mayyasi et al. 2018).

387 Considering the discrepancy of our model and the SPICAM observations, we estimated the hydrogen escape rate
388 during these two Martian years to vary between $\sim 10^{25}$ to $6 \times 10^{26} \text{ s}^{-1}$. This range is in good agreement with the
389 seasonal variations ($3 \times 10^{25} \text{ s}^{-1}$ near aphelion and $4 \times 10^{26} \text{ s}^{-1}$ near perihelion) reported from pick-up protons for the
390 Martian years 32-33 by Rahmati et al. (2018), and from Lyman- α emission by Chaffin et al. (2018) (estimated $\sim 5\text{-}$
391 $14 \times 10^{26} \text{ s}^{-1}$ at $L_s = 250^\circ$ for MY 32 and $1\text{-}4 \times 10^{26} \text{ s}^{-1}$ at $L_s = 200^\circ$ for MY 33). It is slightly lower than the escape rate
392 estimated from the hydrogen column upstream of the bow shock by Halekas (2017); considering $T = 200 \text{ K}$ near
393 aphelion, and $T=300 \text{ K}$ near perihelion, and assuming an uniform escape rate, the escape flux derived from Fig. 5 of
394 Halekas (2017) leads to an escape rate variation from $\sim 3 \times 10^{25}$ to $\sim 3 \times 10^{27} \text{ s}^{-1}$. If we express this escape flux into a
395 water Global Equivalent Layer (GEL) d using

396
$$d(m / Gyr) = \frac{\Phi_H}{2} \frac{m_{H_2O}}{\rho_{H_2O} S} T,$$

397 where $\Phi_H/2$ is the water loss rates, m_{H_2O} the mass of a water molecule, ρ_{H_2O} water mass density, S the Martian surface
398 and T the number of seconds in 1 Gyr ($\sim 3.2 \times 10^{16}$ s/Gyr), we find a loss between ~ 33 to 2000 mm per billion years
399 and therefore no more than 10 m GEL during the last 4 billion years, which is small compared to the total water
400 content measured in the reservoirs at the surface and the subsurface (~ 30 m), and even less compared to the
401 estimated amount of water needed to form the valley networks or outflow channels (estimated to few 100s m GEL
402 with large uncertainties, Lasue et al. 2013). The differences could be either due to a more important hydrogen escape
403 rate in the past or to a larger reservoir of water (ice or liquid) in the subsurface inaccessible or not yet detected by
404 current radar (Orosei et al. 2015, 2018).

405 **6) Conclusion**

406
407 We simulated the atomic hydrogen content in the upper atmosphere of Mars for Martian years 28 and 29. These two
408 years correspond to a period of numerous hydrogen coronal observations by SPICAM on Mars Express. The
409 comparison between our simulated brightness and SPICAM observations shows a reasonable agreement with the
410 observations for $L_s < 200^\circ$ and $L_s > 330^\circ$ for Martian year 28, for $L_s < 150^\circ$ and $L_s > 340^\circ$ for Martian year 29, while
411 the simulated brightness is strongly underestimated for $230 < L_s < 330^\circ$ for Martian year 28 and $270^\circ < L_s < 340^\circ$ for
412 Martian year 29 (therefore, around and after the southern solstice equinox at $L_s=270^\circ$ and the perihelion crossing at
413 $L_s=251^\circ$). This underestimate corresponds to a model underestimate of the global hydrogen density (and the Jeans
414 escape rate) by a factor ~ 6 . Therefore, our study confirms that the seasonal variations of the hydrogen escape at Mars
415 could be of almost two orders of magnitude, as suggested by Chaffin et al. (2014). It also confirms that this variation
416 is a seasonal variation which may be expected every Martian year, as observed from plasma measurements by Mars
417 Express (Yamauchi et al. 2015) and more recently by MAVEN for the Martian year 32, and 33 (e.g., Clarke et al.
418 2017, Halekas 2017, Rahmati et al. 2018, Chaffin et al. 2018). The discrepancy between our simulations and the
419 observations is attributed to an LMD-GCM underestimate of the amount of water vapor transported to high
420 altitudes. Accurate observations of the water vapor density in the Martian upper atmosphere by TGO (Vandaele et
421 al. 2019) or MAVEN/NGIMS could help to better the understanding of the details of this transport.

422 **Acknowledgements**

423

424
425 This project was partially funded by the Programme National de Planetologie and Programme National Soleil Terre
426 and by the Centre National d'Etudes Spatiales. This work has been partially funded by the European Union Horizon
427 2020 Programme (H2020 Compet -08-2014) under grant agreement UPWARDS-633127. We would like to thank G.
428 Lacombe and L. Baggio for their support on the calibration. We thank Allyson Leffler for her careful review of
429 grammatical aspects of this paper. The SPICAM/MEX data used in this study are available through the ESA
430 Planetary Science Archive (PSA, <https://archives.esac.esa.int/psa/>). The monthly average 3D simulated hydrogen
431 exosphere can be found on : <https://owncloud.latmos.ipsl.fr/index.php/s/AdUgv9PdipA2rim>

432
433 **Appendix : List of SPICAM-UV observations used in this study.**
434

435 The list of the SPICAM observations used for the Martian year 28 and 29, and some geometric parameters are given
436 in Table 1 and Table 2 respectively
437

Orbit and Sequence	Date	Ls	Altitude range (km)	SZA range	Latitude range	Slit/No slit	Binning/Y ₀	Band used
3668A1	15 Nov 2006	135.4	600 - 5600	56°	32S	Slit	32/22	5
3838A2	02 Jan 2007	159.8	500- 5500	57°	7N	Slit	32/22	5
3896A1	18 Jan 2007	168.4	600 - 5600	66°	5N	Slit	32/22	5
3988A1	13 Feb 2007	182.9	600-5000	79°	23S	Slit	32/22	5
3989A1	13 Feb 2007	182.9	500 - 4500	79°	37S	Slit	32/22	5
4001A1	17 Feb 2007	185.1	500 - 4800	80°	26S	Slit	32/22	5
4085A1	12 Mar 2007	198.6	1000-4300	39-67	1S – 18S	Slit	32/22	5
4114A1	20 Mar 2007	203.3	900-4600	40-73	12S – 32S	Slit	32/22	5
4178A1	07 Apr 2007	214.3	800 - 4500	50-86	3S – 28S	Slit	32/22	5
4192A1	11 Apr 2007	216.7	500-4100	50-88	4N – 24S	Slit	32/22	5
4215A1	17 Apr 2007	220.4	500-4100	55-93	7N – 22S	Slit	32/22	5
4219A1	18 Apr 2007	221.0	400-3600	57-92	19N – 13S	Slit	32/22	5
4407A4	10 Jun 2007	254.4	500-4000	10-80	14S – 54N	Slit	32/118	4
4475A1	29 Jun 2007	266.5	400 -4200	36-86	4S – 58N	Slit	32/118	4
4501A1	07 Jul 2007	271.5	900 - 4300	14-67	14S – 44N	No Slit	32/118	1

4577A3	28 Jul 2007	284.6	1100-4800	8 -60	16S – 34N	Slit	32/118	4
4646A1	16 Aug 2007	296.2	1300-5600	58	28N	Slit	32/118	4
4671A2	23 Aug 2007	300.4	1100-5100	47°	10N	No Slit	32/118	1
4673A2	24 Aug 2007	301.0	1300-5500	51°	17N	Slit	32/118	4
4693A2	29 Aug 2007	304.0	300 -10000	36-96	5N – 76N	Slit	32/118	4
4729A1	08 Sep 2007	309.8	1100-3500	45°	23S	No slit	32/118	1
4740A1	11 Sep 2007	311.6	1100 - 3600	47°	25S	Slit	32/118	4
4757A2	16 Sep 2007	314.5	700 - 3600	50°	28S	No slit	32/118	1
4769A2	20 Sep 2007	316.8	300-10000	19-85	1S - 63N	Slit	32/118	4
4772A2	20 Sep 2007	316.8	700 – 3600	53	31S	Slit	32/118	4
4785A1	24 Sep 2007	319.1	700 – 3600	56	33S	Slit	32/118	4
4794A2	27 Sep 2007	320.8	800 - 10000	19 - 90	2N – 60N	Slit	32/118	4
4796A1	27 Sep 2007	320.8	700 - 3600	57	34S	No Slit	32/118	1
4856A1	14 Oct 2007	330.2	700 – 3600	69	45S	No Slit	32/118	1
4903A1	27 Oct 2007	337.3	1400-5500	76	23S	No Slit	32/118	1
4905A1	28 Oct 2007	337.8	700 - 5600	77	10S	Slit	32/118	4
4910A1	29 Oct 2007	338.4	1000-5600	77	17S	No Slit	32/118	1
4914A1	30 Oct 2007	338.9	1000-5600	78	18S	Slit	32/118	4
4923A1	02 Nov 2007	340.5	700-5000	79	34S	No Slit	32/118	1
4950A1	09 Nov 2007	344.2	700-5000	84	39S	Slit	32/118	4
5005A1a	25 Nov 2007	352.5	300-3300	32-56	24S – 9N	Slit	32/118	4
5016A1	28 Nov 2007	354.0	600-3600	35-59	14S – 14N	Slit	32/118	4
5024A1	30 Nov 2007	355.1	500-3700	34-61	17N – 29N	Slit	32/118	4
5052A1	08 Dec 2007	359.1	500-3900	36-66	18N – 31N	Slit	32/118	4

438 *Table 1 : List of SPICAM-UV observations used to study the Martian hydrogen corona during the Martian year 28.*
439 *The orbit number and sequence number of the observations are given in column 1. Column 3 gives the approximate*
440 *solar longitude Ls at the observation day. Columns 4 and 5 refer to the tangent point of the line of sight.*

441
442

Orbit and Sequence	Date	Ls	Altitude range	SZA range	Latitude range	Slit/No slit	Binning/Y	Band used
5070A1	13 Dec 2007	1.6	800-4300	41-70	15N – 29N	Slit	32/118	4
5097A1	21 Dec 2007	5.5	900-10,000	75-107	0 – 60N	Slit	32/118	4
5119A1	27 Dec 2007	8.5	1000-4800	50-80	16N – 32N	Slit	32/118	4

5122A1	28 Dec 2007	8.9	1000-4500	50-80	7N – 25N	No Slit	32/118	1
5129A1	30 Dec 2007	9.9	900-4400	50-80	4N – 22N	Slit	32/118	4
5135A1	31 Dec 2007	10.4	900-4600	50-82	14N – 33N	Slit	32/118	4
5154A1	06 Jan 2008	13.3	950-4500	55-85	0 – 20N	Slit	32/118	4
5156A1	06 Jan 2008	13.3	1100-4900	56-87	13N – 32N	Slit	32/118	4
5266A1	07 Feb 2008	28.3	450-4300	40-99	23S – 85S	Slit	32/118	4
5283A1	12 Feb 2008	30.6	700-4500	48-99	34S – 71S	No Slit	32/118	1
5290A2	14 Feb 2008	31.5	700-4500	48-99	34S – 72S	Slit	32/118	4
5304A1	18 Feb 2008	33.3	600-4400	40-97	22S – 83S	No Slit	32/118	1
5341A1	28 Feb 2008	37.9	600-4400	35-95	19S – 78S	Slit	32/118	4
5353A1	03 Mar 2008	39.7	500-4300	31-92	14S – 76S	No Slit	32/118	1
5367A1	07 Mar 2008	41.5	500-4400	33-93	16S – 75S	Slit	32/118	4
5374A1	09 Mar 2008	42.4	500-4300	30-92	12S – 73S	No Slit	32/118	1
5388A1	13 Mar 2008	44.2	600-4000	52-101	29S – 59S	Slit	32/118	4
5390A1	13 Mar 2008	44.2	600-4000	52-101	28S – 59S	No Slit	32/118	1
5404A1	17 Mar 2008	45.9	600-4000	50-100	26S – 62S	Slit	32/118	4
5416A1	21 Mar 2008	47.7	600-4100	47-98	22S – 64S	No Slit	32/118	1
5432A1	25 Mar 2008	49.5	600-4100	46-98	21S – 65S	Slit	32/118	4
5446A1	29 Mar 2008	51.3	600-4200	43-95	17S – 66S	No Slit	32/118	1
5462A1	03 Apr 2008	53.5	600-4000	51-100	21S – 63S	Slit	32/118	4
5546A1	27 Apr 2008	64.0	400-3600	57-100	12S – 59S	Slit	32/118	4
5617A2	17 May 2008	72.7	500-4000	40-77	14N – 43S	Slit	32/118	4
5662A2	30 May 2008	78.4	400-3900	35-70	17N – 39S	Slit	32/118	4
5715A2	14 Jun 2008	85.0	800-3400	60-91	12S – 46S	No Slit	32/118	1
5726A2	17 Jun 2008	86.3	900-3300	58-89	11S – 45S	No Slit	32/118	1
5759A2	26 Jun 2008	90.7	300-1900	30-70	23N – 31S	Slit	32/118	4
6168A1*	21 Oct 2008	144.9	730-200-1200	105-48-49	52S – 61N	Slit	32/23	5
6200A1*	30 Oct 2008	149.4	900-200-1300	101-51-55	64S – 61N	Slit	32/23	5
6206A1*	01 Nov 2008	150.5	1200-200-1300	95-59-64	73S – 60N	Slit	32/23	5
6213A1*	03 Nov 2008	151.5	900-200-1300	100-50-55	66S – 60N	Slit	32/23	5
6440A1	07 Jan 2009	187.0	900-110-1200	87-72-78	73S – 23N	Slit	32/118	4
6478A1*	18 Jan 2009	193.3	1200-200-600	100-46-49	23S-61S-16S	Slit	32/118	4

6521A1	30 Jan 2009	200.6	1300-100-1200	130-35	40S-73S-2S	Slit	32/118	4
6546A1*	06 Feb 2009	204.9	1300-200-1100	120-28	27S-65S-13S	Slit	32/118	4
6593A1*	20 Feb 2009	213.1	1100-200-500	120-44	3S-72S-42S	Slit	32/118	4
6666A1	13 Mar 2009	226.1	1300-100-1300	140-12	19S-74S-23S	Slit	32/118	4
6691A3*	20 Mar 2009	230.4	1300-200-1300	140-13	14S-66S-26S	Slit	32/118	4
6722A1*	29 Mar 2009	236.2	1300-200-1300	150-20	9S-67S-31S	Slit	32/118	4
6765A1	10 Apr 2009	244.1	900-100-1200	135-10	18S-70S-24S	Slit	32/118	4
6801A1	20 Apr 2009	250.0	1300-100-1200	140-35	7N-77S-27S	Slit	32/118	4
6832A1	29 Apr 2009	256.3	800-100-1200	140-10	9S-66S-32S	Slit	32/118	4
6859A1	07 May 2009	261.2	900-90-1200	140-15	2S-66S-39S	Slit	32/118	4
6888A1	15 May 2009	266.5	900-90-1200	140-20	3N-65S-43S	Slit	32/118	4
6895A1	17 May 2009	267.7	900-90-1200	140-20	4N-65S-44S	Slit	32/118	4
6949A1	02 Jun 2009	277.5	1300-10-900	150-65	42N – 87S	Slit	32/118	4
6956A2	04 Jun 2009	278.4	1300-10-900	150-65	43N – 87S	Slit	32/118	4
6960A1	05 Jun 2009	279.	1300-10-800	144-74	41N – 81S	Slit	32/118	4
6967A1	07 Jun 2009	280.3	1300-10-800	145-75	42N – 80S	Slit	32/118	4
7045A2&3	29 Jun 2009	294.	3300-8500-7700	64-84	19S – 14S	Slit	32/118	4
7046A1&2 ⁺	30 Jun 2009							
7089A3&4	12 Jul 2009	301.6	2900-9200-8800	70-89	20S – 14S	Slit	32/118	4
7090A1&2	12 Jul 2009							
7122A2&3	22 Jul 2009	307.5	2400-9600-9300	73-94	21S – 15S	Slit	32/118	4
7123A1&2	22 Jul 2009							
7292A1	08 Sep 2009	334.6	2500-4000	53-58	58S – 40S	Slit	32/118	4
7293A1	09 Sep 2009	335.2	2800-4300	54-59	57S – 39S	Slit	32/118	4
7320A2	17 Sep 2009	339.5	2100-4100	56-63	67S – 52S	Slit	32/118	4
7321A2	17 Sep 2009	339.5	2400-4300	57-63	67S – 52S	Slit	32/118	4
7421A1	16 Oct 2009	354.6	4200-5600	78	74S	Slit	32/118	4
7423A1	16 Oct 2009	354.6	200-3000	76	76S	Slit	32/118	4
7446A1	23 Oct 2009	358.1	4400-6200	81	73S	Slit	32/118	4
7447A3	23 Oct 2009	358.1	4500-6300	80	73S	Slit	32/118	4

443 *Table 2 : List of SPICAM-UV observations used to study the Martian hydrogen corona during the Martian year 29.*
444 *The orbit number and sequence number of the observations are given in column 1. Column 3 gives the approximate*
445 *solar longitude Ls at the observation day. Columns 4, 5 and 6 refer to the tangent point of the line of sight. *For*
446 *these observations solar scattered light is observed at low altitudes on all bands polluting the airglow emissions.*

447 *Only altitudes above ~200 km are considered in these cases.*

448
449
450
451
452
453
454
455
456
457
458
459
460
461
462
463
464
465

466

467 **References**

468

469 Bertaux, J-L., O. Korablev, S. Perrier, E. Quémerais, F. Montmessin, F. Leblanc, S. Lebonnois, P. Rannou, F.

470 Lefevre, F. Forget, A. Fedorova, E. Dimarellis, A. Reberac, D. Fonteyn, J-Y. Chaufray, and S. Guibert,

471 SPICAM on Mars Express : Observing modes and overview of UV spectrometer data and scientific results, J.

472 Geophys. Res., 111, E10S90, doi:10.1029/2006JE002690, 2006

473 Bertucci, C., N. Romanelli, J-Y. Chaufray, D. Gomez, C. Mazelle, M. Delva, R. Modolo, F. Gonzalez-Galindo, and

474 D.A. Brain, Temporal variability of waves at the proton cyclotron frequency upstream from Mars :

475 Implication for Mars distant hydrogen exosphere, Geophys. Res. Lett., 40, 3809-3813, doi:10.1002/grl.50709,

476 2013

477 Beth, A., P. Garnier, D. Toublanc, I. Dandouras, and C. Mazelle, (2016), Theory for planetary exospheres : II

478 Radiation pressure effect on exospheric density profiles, Icarus, 266, 423- 432

479 Bhattacharyya, D., J.T. Clarke, J-L. Bertaux, J-Y. Chaufray, M.Mayyasi, (2015), A strong seasonal dependence in the

480 martian hydrogen exosphere, Geophys. Res. Lett., 42, 8678- 868

481 Bhattacharyya, D., J.T. Clarke, J-L. Bertaux, J-Y. Chaufray, and M. Mayyasi, (2017) Analysis and modeling of

482 remote observations of the martian hydrogen exosphere, Icarus, 281, 264-280

483 Bibring, J-P., Y. Langevin, J. Mustard, F. Poulet, R. Arvidson, A. Gendrin, B. Gondet, N. Mangold, P. Pinet, F.

484 Forget, and the OMEGA team, Global Mineralogical and Aqueous history of Mars derived from

485 OMEGA/Mars Express data, *Science*, 312, 400-404, (2006)

486 Bishop, J., et al., Phyllosilicate diversity and past aqueous activity revealed at Mawrth Vallis, Mars, *Science*, 321,
487 830-833, doi : 10.1126/science.1159699, (2008)

488 Boqueho, V., and P-L. Blelly, Contributions of a multimoment multispecies approach in modeling planetary
489 atmospheres: Example of Mars, *J. Geophys. Res.*, 110, A01313, doi: 10.1029/2004JA010414, 2005

490 Brinkmann, R.T., Departures from Jeans' escape rate for H and He in the Earth's atmosphere, (1970), *Planet. Space*
491 *Sci.*, 18, 449-478

492 Chaffin, M.S., J-Y. Chaufray, I.A.F Stewart, F. Montmessin, N.M. Schneider, and J-L. Bertaux, (2014), Unexpected
493 variability of Martian hydrogen escape, *Geophys. Res. Lett.*, 41, 314- 320, doi: 10.1002/2013GL058578

494 Chaffin, M.S., J. Deighan, N.M. Schneider, and A.I.F. Stewart, Elevated atmospheric escape of atomic hydrogen
495 from Mars induced by high-altitude water, *Nat. Geosc.*, 10, 174-178, (2017)

496 Chaffin, M.S., J-Y. Chaufray, J. Deighan, N.M. Schneider, M. Mayyasi, J.T. Clarke, E. Thiemann, S.K. Jain, M.M.J.
497 Crismani, A. Stiepen, F.G. Eparvier, W.E. McClintock, A.I.F. Stewart, G.M. Holsclaw, F. Montmessin, and
498 B.M. Jakosky, Mars H escape rates derived from MAVEN/IUVS Lyman- α brightness measurements and their
499 dependence on model assumptions, *J. Geophys. Res: Planets*, 123, 2192-2210, doi: 10.1029/2018JE005574,
500 (2018)

501 Chaufray, J-Y., J-L. Bertaux, F. Leblanc, and E. Quémerais, (2008), Observation of the hydrogen corona with
502 SPICAM on Mars Express, *Icarus*, 195, 598-613

503 Chaufray, J-Y., F. Leblanc, E. Quémerais, and J-L. Bertaux, Martian oxygen density at the exobase deduced from OI
504 130.4 nm observations by SPICAM on Mars Express, *J. Geophys. Res.*, 114, E02006,
505 doi:10.1029/2008JE003130, 2009

506 Chaufray, J-Y., J-L. Bertaux, E. Quémerais, E. Villard, F. Leblanc, Hydrogen density in the dayside venusian
507 exosphere derived from Lyman- α observations by SPICAV on Venus Express, *Icarus*, 217, 767-778, 2012

508 Chaufray, J-Y., F. Gonzalez-Galindo, F. Forget, M.A. Lopez-Valverde, F. Leblanc, R. Modolo, and S. Hess, (2015a),
509 Variability of the hydrogen in the martian upper atmosphere as simulated by a 3D atmosphere-exosphere
510 coupling, *Icarus*, 245, 282-294

511 Chaufray, J-Y., J-L. Bertaux, F. Leblanc, E. Quémerais, and S. Sulis, (2015b), Observations of the nightside venusian
512 hydrogen corona with SPICAV/VEX, *Icarus*, 262, 1-8

513 Chaufray, J-Y., F. Gonzalez-Galindo, F. Forget, M.A. Lopez-Valverde, F. Leblanc, R. Modolo, and S. Hess, (2017),
514 Reply to comment « On the hydrogen escape: Comment to Variability of the hydrogen in the Martian upper
515 atmosphere as simulated by a 3D atmosphere-exosphere coupling by J-Y Chaufray et al.” by V.
516 Krasnopolsky, *Icarus*, 281, 262, doi : 10.1016/j.icarus.2017.07.013

517 Chaufray, J-Y., R.V. Yelle, F. Gonzalez-Galindo, F. Forget, M. Lopez-Valverde, F. Leblanc, R. Modolo, (2018),
518 Effect of the lateral exospheric transport on the horizontal hydrogen distribution at the exobase of Mars, *J.*
519 *Geophys. Res.*, 123, 4241-4254, doi : 10.1002/2017JA025163

520 Clancy, R.T., B.J. Sandor, M.J. Wolff, P.R. Christensen, M.D. Smith, J.C. Pearl, B.J. Conrath, and R.J. Wilson, An
521 intercomparison of ground-based millimeter, MGS TES, and Viking atmospheric temperature measurements:
522 Seasonal and interannual variability of temperatures and dust loading in the global Mars atmosphere, *J.*
523 *Geophys. Res.*, 105, 9553-9571, 2000

524 Clarke, J. T., J-L. Bertaux, J-Y. Chaufray, G.R. Gladstone, E. Quémerais, J.K. Wilson, and D. Bhattacharyya, A rapid
525 decrease of the hydrogen corona of Mars, *Geophys. Res. Lett.*, 41, 8013-8020, 2014

526 Clarke, J.T., M. Mayyasi, D. Bhattacharyya, N.M. Schneider, W.E. McClintock, J.I. Deighan, A.I.F. Stewart, J-Y.
527 Chaufray, M.S. Chaffin, S.K. Jain, A. Stiepen, M. Crismani, G.M. Holsclaw, F. Montmessin, and B. Jakosky,
528 Variability of D and H in the Martian upper atmosphere observed with the MAVEN IUVS echelle channel, *J.*
529 *Geophys. Res.*, 122, 2336-2344, doi: 10.1002/2016JA023479

530 Emerich, C., P. Lemaire, J-C. Vial, W. Curdt, U. Schüle, K. Wilhelm, A new relation between the central spectral
531 solar H I Lyman α irradiance and the line irradiance measured by SUMER/SOHO during the cycle 23., *Icarus*,
532 178, 429-433, (2005)

533 Fedorova, A., J-L. Bertaux, D.Betsis, F. Montmessin, O. Korablev, L. Maltagliati, and J. Clarke, Water vapor in the
534 middle atmosphere of Mars during the 2007 global dust storm, *Icarus*, 300, 440, 2018

535 Forget, F., F. Hourdin, R. Fournier, C. Hourdin, O. Talagrand, M. Collins, S.R. Lewis, P.L. Read, J-P. Huot,
536 Improved general circulation models of the Martian atmosphere from the surface to above 80 km, *J. Geophys.*
537 *Res.*, 104, 24,155-24,175, 1999

538 Fox J.L., M. Benna, P.R. Mahaffy, and B.M. Jakosky, Water and water ions in the Martian thermosphere/ionosphere,
539 *Geophys. Res. Lett.*, 42, 8977-8985, doi: 10.1002/2015GL065465, (2015)

540 Gladstone, G.R., Auroral resonance line radiative transfer, *J. Geophys. Res.*, 97, 1377-1387, 1992

541 Gonzalez-Galindo, F., F. Forget, M.A. Lopez-Valverde, M. Angelats i Coll, and E. Millour, A ground-to-exosphere
542 Martian general circulation model: 1 Seasonal, diurnal, and solar cycle variation of thermospheric
543 temperatures, *J. Geophys. Res.*, 114, E04001, doi:10.1029/2008JE003246, 2009

544 Gonzalez-Galindo, F., M.A. Lopez-Valverde, F. Forget, M. Garcia-Comas, E. Millour, and L. Montabone, (2015),
545 Variability of the Martian thermosphere during eight Martian years as simulated by a ground-to-exosphere
546 global circulation model, *J. Geophys. Res.*, 120, 2020-2035, doi:10.1002/2015JE004925

547 Halekas, J. S. (2017), Seasonal variability of the hydrogen exosphere of Mars, *J. Geophys. Res. Planets*, 122,
548 doi:10.1002/2017JE005306

549 Heavens et al, Hydrogen escape from Mars enhanced by deep convection in dust storms, *Nature Astronom.*, 2, 126–
550 132 (2018)

551 Hynek, B.M., M. Beach, and M.R.T. Hoke, Updated global map of Martian valley networks and implications for
552 climate and hydrologic processes, *J. Geophys. Res.*, 115, E09008, doi: 10.1029/2009JE003548, (2010)

553 Jakosky, B. et al., Loss of the Martian atmosphere to space: Present-day loss rates determined from MAVEN
554 observations and integrated loss through time, *Icarus*, 315, 146-157, (2018)

555 Krasnopolsky, V., Mars' upper atmosphere and ionosphere at low, medium, and high solar activities: Implications for
556 evolution of water, *J. Geophys. Res.*, 107(E12), 5128, doi: 10.1029/2001JE001809, 2002

557 Krasnopolsky, V., Solar activity variations of thermospheric temperatures on Mars and a problem of CO in the lower
558 atmosphere, *Icarus*, 207, 638-647, (2010)

559 Krasnopolsky, V., On the hydrogen escape from Mars: comments to “Variability of the hydrogen in the Martian
560 upper atmosphere as simulated by a 3D atmosphere-exosphere coupling” by JY Chaufray et al., *Icarus*, 281,
561 262-263, (2017)

562 Krasnopolsky, V.A., Photochemistry of water in the martian thermosphere and its effect on hydrogen escape, *Icarus*,
563 321, 62-70, 2019

564 Lasue, J., N. Mangold, E. Hauber, S. Clifford, W. Feldman, O. Gasnault, C. Grima, S. Maurice, and O. Mousis,
565 Quantitative assessments of the Martian hydrosphere, *Space Sci. Rev.*, 174, 155-212, (2013)

566 Leblanc, F., J-Y. Chaufray, J. Lilensten, O. Witasse, and J-L. Bertaux, Martian dayglow as seen by the SPICAM UV
567 spectrograph on Mars Express, *J. Geophys. Res.*, 111, E09S11, doi: 10.1029/2005JE002664, 2006

568 Lee, J.S., Refined Monte Carlo method for simulating angle-dependent partial frequency redistributions, *Astrophys.*

569 J., 255, 303-306, 1982

570 Lopez-Valverde, M.A. et al., Investigation of the Mars upper atmosphere with ExoMars Trace Gas Orbiter, Space
571 Sci. Rev., 214:29, doi: 10.1007/s11214-017-0463-4, (2018)

572 Maltagliati, L., F. Montmessin, O. Korablev, A. Fedorova, F. Forget, A. Määttänen, F. Lefèvre, and J-L. Bertaux,
573 (2013) Annual survey of water vapor vertical distribution and water- aerosol coupling in the martian
574 atmosphere observed by SPICAM/Mex solar occultations, *Icarus*, 223, 942-962

575 Mayyasi, M., D. Bhattacharyya, J. Clarke, A. Catalano, M. Benna, P. Mahaffy, E. Thiemann, C. Lee, J. Deighan, J.
576 Sonal, and 9 co-authors, (2018), Significant space weather impact on the escape of hydrogen from Mars,
577 *Geophys. Res. Lett.*, 45, 8844

578 Montabone, L., F. Forget, E. Millour, R.J. Wilson, S.R. Lewis, B. Cantor, D. Kass, A. Kleinbohl, M.T. Lemmon,
579 M.D. Smith, M.J. Wolff, Eight-year climatology of dust optical depth on Mars, *Icarus*, 251, 65-95, 2015

580 Montmessin, F., F. Forget, P. Rannou, M. Cabane, R. M. Haberle, Origin and role of water ice clouds in the Martian
581 water cycle as inferred from a general circulation model, *J. Geophys. Res.*, 109, E10004, doi :
582 10.1029/2004JE002284, 2004

583 Montmessin, F., O. Korablev, F. Lefevre, J-L. Bertaux, A. Fedorova, A. Trokhimovskiy, J-Y. Chaufray, G. Lacombe,
584 A. Reberac, L. Maltagliati, Y. Willame, S. Guslyakova, J-C. Gerard, A. Stiepen, D. Fussen, N. Mateshvili, A.
585 Maatanen, F. Forget, O. Witasse, F. Leblanc, A.C. Vandaele, E. Marcq, B. Sandel, B. Gonder, N. Schneider,
586 M Chaffin, N. Chapron, SPICAM on Mars Express: A 10 year in-depth survey of the Martian atmosphere,
587 *Icarus*, 297, 195-216, 2017

588 Navarro, T., J.-B. Madeleine, F. Forget, A. Spiga, E. Millour, F. Montmessin, and A. Määttänen. Global climate
589 modeling of the Martian water cycle with improved microphysics and radiatively active water ice clouds.
590 *Journal of Geophysical Research (Planets)*, 119:1479- 1495, 2014

591 Orosei, R., R.L. Jordan, D.D Morgan, M. Cartacci, A. Cicchetti, F. Duru, D.A. Gurnett, E. Heggy, D.L. Kirchner, R.
592 Noschese, W. Kofman, A. Masdea, J-J. Plaut, R. Seu, T.R. Watters, G. Picardi, Mars Advanced Radar for
593 subsurface and ionospheric sounding (MARSIS) after nine years of operation : A summary, *Planet Space Sci.*,
594 112, 98-114, (2015)

595 Orosei, R., S.E. Lauro, E. Pettinelli, A. Cicchetti, M. Coradini, B. Cosciotti, F. Di Paolo, E. Flamini, E. Mattei, M.
596 Pajola, and 12 co-authors, Radar evidence of subglacial liquid water on Mars, *Science*, 361, 490, (2018)

597 Quémerais, E., Angle dependent partial frequency redistribution in the interplanetary medium at Lyman- α , *Astron.*
598 *Astrophys.*, 358, 353-367, 2000

599 Rahmati, A., D.E. Larson, T.E. Cravens, R.J. Lillis, J.S. Halekas, J.P. McFadden, D.L. Mitchell, E.M.B. Thiemann,
600 J.E.P. Connerney, P.A. Dunn, C.O. Lee, F.G. Eparvier, G.A. DiBraccio, J.R. Espley, J.G. Luhmann, C.
601 Mazelle, and B.M. Jakosky, Seasonal variability of neutral escape from Mars as derived from MAVEN
602 pickup ion observations, *J. Geophys. Res. : Planets*, 123, 1192-1202, 10.1029/2018JE005560, (2018)

603 Romanelli, N. C. Mazelle, J-Y. Chaufray, K. Meziane, L. Shan, S. Ruhunusiri, J.E.P. Connerney, J. R. Espley, F.
604 Eparvier, T.E. Thiemann, et al., 2016, Proton cyclotron, waves occurrence rate upstream from Mars observed
605 by MAVEN : Associated variability of the Martian upper atmosphere, *J. Geophys. Res.*, 121, 11,113-11,128,
606 doi : 10.1002/2016JA023270

607 Rottman, G.J., N.W. Thomas; W. McClintock, *SORCE solar UV irradiance results*, *Adv. Space Sci.*, 37, 201-208,
608 (2006)

609 Shaposhnikov, D.S., A.S. Medvedev, A.V. Rodin, and P. Hartogh, Seasonal water “pump” in the atmosphere of
610 Mars: Vertical transport to the thermosphere, *Geophys. Res. Lett.*, 46, 4161-4169, (2019)

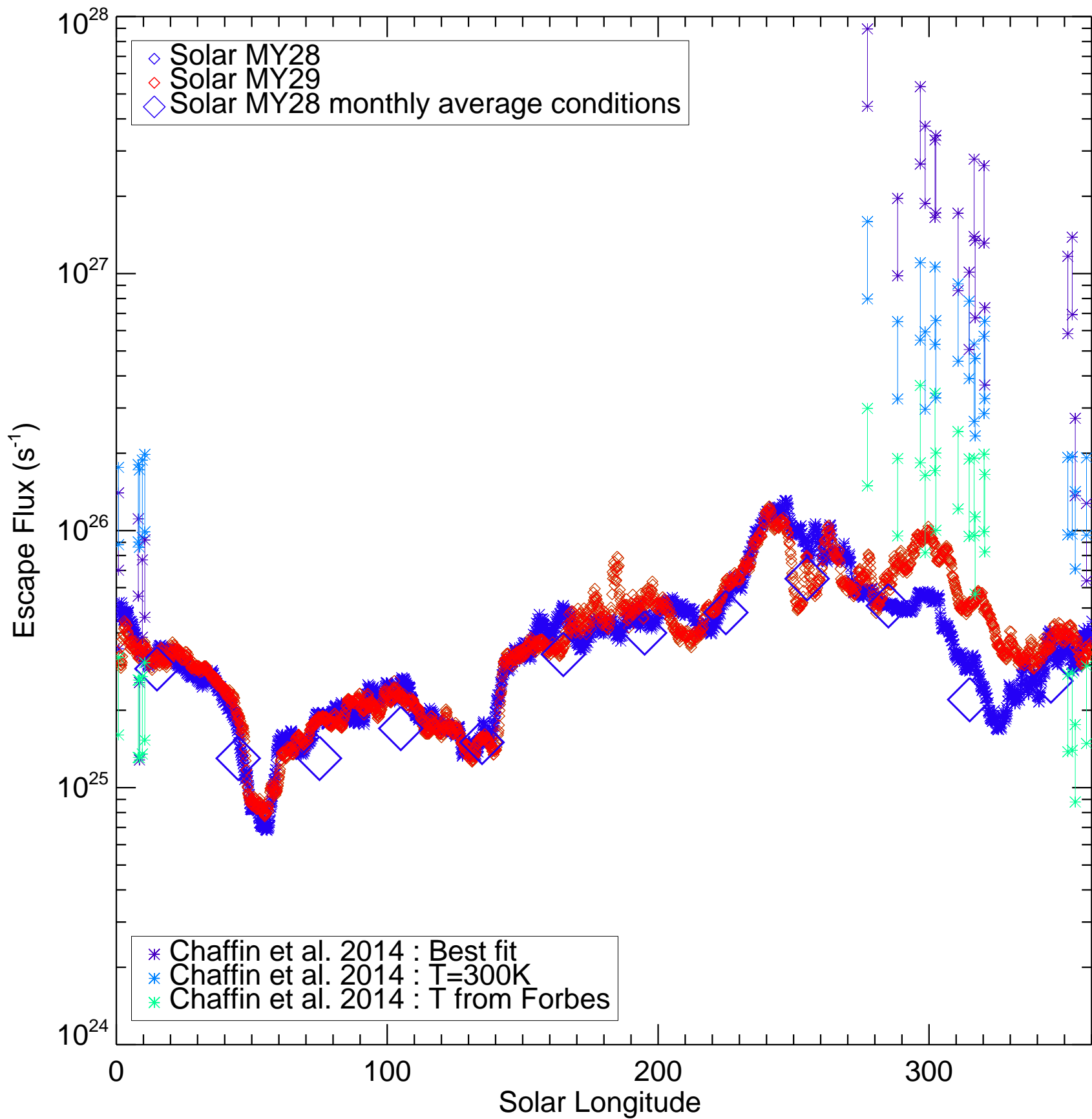
611 Shizgal, B., and R. Blackmore, A collisional kinetic theory of a plane parallel evaporating planetary atmosphere,
612 *Planet. Space Sci.*, 34, 279-291, (1986).

613 Terada, K., N. Terada, H. Shinagawa, H. Fujiwara, Y. Kasaba, K. Seki, F. Leblanc, J-Y. Chaufray, and R. Modolo, A
614 full-particle Martian upper thermosphere-exosphere model using the DSMC method, *J. Geophys. Res.*, 121,
615 1429-1444, doi: 10.1002/2015JE004961, 2016

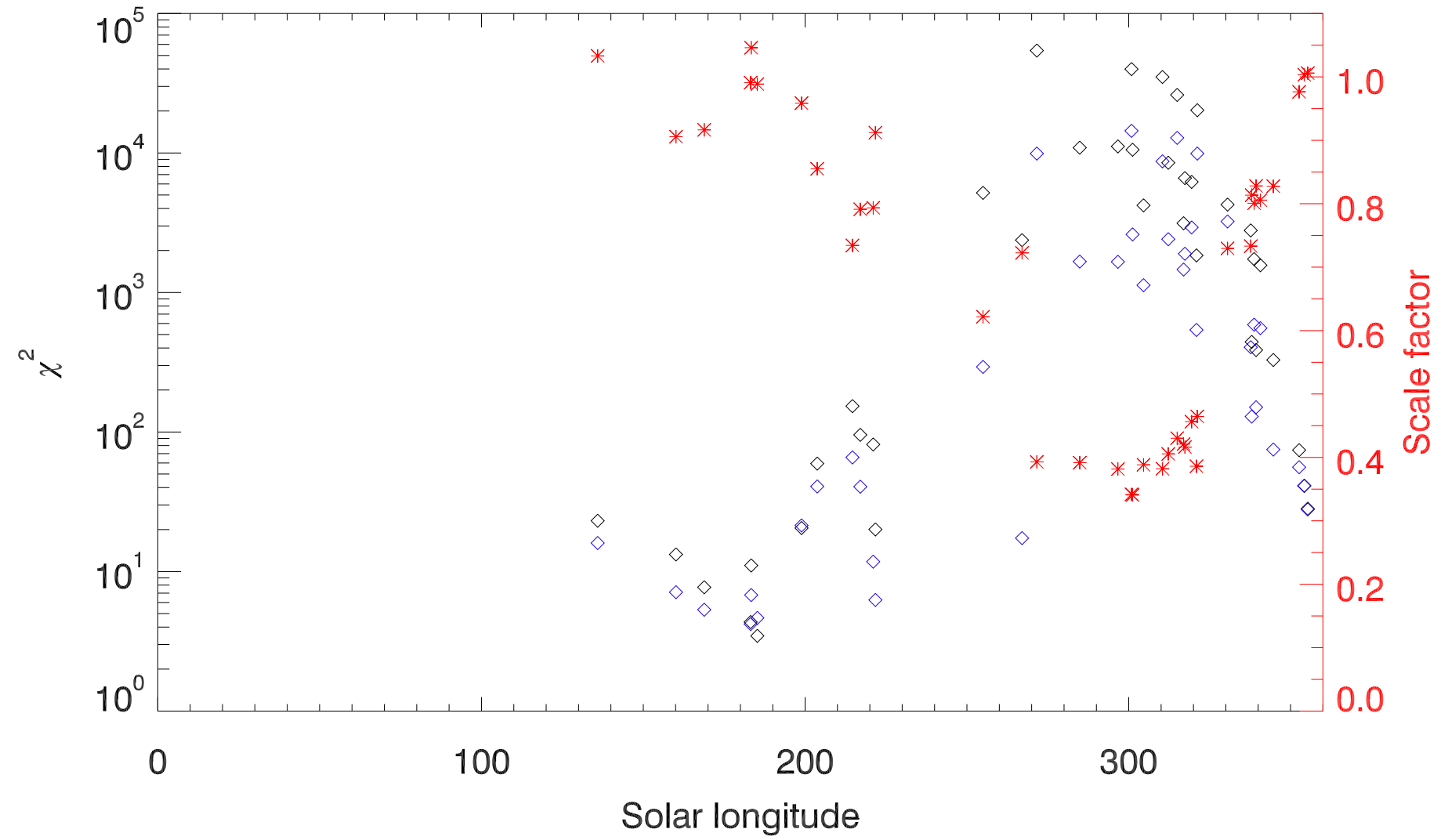
616 Vandaele, A.C, O. Korablev, F. Daerden, et al., Martian dust storm impact on atmospheric H₂O and D/H observed by
617 ExoMars Trace Gas Orbiter, *Nature*, 568, 52, (2019)

618 Vidal-Madjar, A., and J-L. Bertaux, A calculated hydrogen distribution in the exosphere, *Planet Space Sci.*, 20, 1147-
619 1162, 1972

620 Yamauchi, M., T. Hara, R. Lundin, E. Dubinin, A. Fedorov, J-A. Sauvaud, R.A. Frahm, R. Ramstad, Y. Futaana, M.
621 Holmstrom, S. Barabash (2015), Seasonal variation of martian pick-up ions: Evidence of breathing exosphere,
622 *Planet. & Sp. Sci.*, 119, p. 54



Martian year 28



Martian year 29

